Optical Response of Subwavelength Gratings and Photonic Crystals in Silicon Photonic Devices and Centric Diatoms

Santiago Bernal

Department of Electrical & Computer Engineering

McGill University, Montreal

August 2022

A thesis submitted to McGill University in the partial fulfillment of the requirements of the degree of Master of Engineering

Abstract

The ever-growing information and communications technology (ICT) sector supports the demands of higher internet traffic and speeds. This has prompted an accelerated growth of optical interconnects which are ever changing to comply with the demands for faster, cheaper, as well as more energy efficient and sustainable devices. The Silicon photonics (SiP) technology can deal with these demands. It leverages the mature complementary metal-oxide-semiconductor (CMOS) fabrication process flow to produce cost-effective solutions. Recently, new techniques have been incorporated into the designs of these devices to reduce their footprint and increase their bandwidth. These include the use of subwavelength gratings (SWG) and photonic crystals (PhC) structures which enable dispersion and birefringence engineering in nanophotonic devices and in nature. In the first part of this thesis, we review the concepts behind SWGs and PhCs by linking their optical behaviour and design principles to band diagram simulations.

In the second part of this thesis, we report the use of SWGs to design a compact low-loss one by two multi-mode interferometer (MMI) operating as a power splitter over the telecommunication C-band and O-band. The device bandwidth was simulated to be over 100 nm for both TE and TM modes. The simulated insertion loss (IL) for TE modes was found to be around 0.1 dB across the entire bandwidth, while for TM modes, it ranged from 0.45 dB to 0.63 dB. However, experimental results revealed a higher TE IL of 0.54 dB and 0.96 dB at 1310 nm and 1550 nm, respectively. The experimental imbalance between the two output ports ranged from 1.09 dB to 0.73 dB for TE devices in the O-band and C-band.

In the third part of this thesis, we examine the use of PhCs found on the glass-like shell of diatoms, a species of unicellular phytoplankton. These shells, called frustules, are the result of millions of years of evolution and their understanding could lead to new sustainable applications

of light harvesting and retention mechanisms. Their optical response was analyzed by using an experimental characterisation procedure consisting of scanning electron microscopy (SEM), scanning near-field optical microscopy (SNOM), and atomic force microscopy (AFM), as well as by investigating the photonic band structure in relation with peaks in the absorption spectrum of the chloroplast found in a centric diatom species known as Cyclotella Quillensis (CQ).

Résumé

Le secteur en croissance constante des technologies de l'information et des communications (TIC) répond aux exigences de plus en plus élevées du trafic et de la vitesse de l'Internet. Cela a entraîné une croissance accélérée des interconnexions optiques qui évoluent constamment pour répondre aux demandes de dispositifs plus rapides, moins chers, plus économes en énergie et plus durables. La technologie de la photonique sur silicium (SiP) peut répondre à ces demandes. Elle exploite le flux de processus de fabrication de métal-oxyde-semi-conducteur complémentaire (CMOS) mature pour produire des solutions rentables. Récemment, de nouvelles techniques ont été intégrées dans la conception de ces appareils pour réduire leur encombrement et augmenter leur bande passante. Celles-ci incluent l'utilisation de réseaux de sous-longueur d'onde (SWG) et de structures de cristaux photoniques (PhC) qui permettent l'ingénierie de dispersion et de biréfringence dans les dispositifs nanophotoniques et dans la nature. Dans la première partie de cette thèse, nous passons en revue les concepts derrière les SWG et les PhC en liant leur comportement optique et leurs principes de conception a des simulations de diagramme de bande.

Dans la deuxième partie de cette thèse, nous présentons l'utilisation des SWG pour concevoir un interféromètre multimode (MMI) compact à faible perte fonctionnant comme un répartiteur de puissance sur la bande C et la bande O des télécommunications. La bande passante de l'appareil a été simulée pour être supérieure à 100 nm pour les modes TE et TM. La perte d'insertion simulée (IL) pour les modes TE est d'environ 0,1 dB sur toute la bande passante, tandis que pour les modes TM, elle variait de 0,45 dB à 0,63 dB. Cependant, les résultats expérimentaux ont révélé un TE IL plus élevé de 0,54 dB et 0,96 dB à 1310 nm et 1550 nm, respectivement. Le

déséquilibre expérimental entre les deux ports de sortie variait de 1,09 dB à 0,73 dB pour les dispositifs TE dans la bande O et la bande C.

Dans la troisième partie de cette thèse, nous examinons l'utilisation des PhC trouvés sur la coquille vitreuse des diatomées, une espèce de phytoplancton unicellulaire. Ces coquilles, appelées frustules, sont le résultat de millions d'années d'évolution et leur compréhension pourrait conduire à de nouvelles applications durables des mécanismes de récupération et de rétention de la lumière. Leur réponse optique a été analysée à l'aide d'une procédure de caractérisation expérimentale consistant en la microscopie électronique à balayage (SEM), la microscopie optique en champ proche (SNOM) et la microscopie à force atomique (AFM), ainsi qu'en étudiant la structure de la bande photonique en relation avec les pics dans le spectre d'absorption du chloroplaste trouvés dans une espèce de diatomée centrée connue sous le nom de Cyclotella Quillensis (CQ).

Acknowledgements

I would first like to thank my supervisor, Professor David Plant, for his continuous support, guidance, and advice throughout my graduate studies. Ever since I joined his group as a summer intern, he has welcomed me and allowed me to work along side his top students. I will forever be grateful for the resources and time he invested in me.

I would also like to thank Yannick D'Mello for his friendship, his mentorship, and most importantly, his patience. Yannick was the first graduate student who took the time and effort to teach me and guide me through the many ups and downs of graduate school. I am honored to have had the chance to work alongside him on so many diverse projects.

I want to express my deepest thanks to Dr. Dan Petrescu whose teachings and contributions made the phytoplankton project possible. He was an enthusiastic collaborator and a good friend.

Additionally, I thank the entirety of the photonics system group members who helped me throughout my studies. I am especially grateful to James Skoric, Galib Hakim, Deng Mao, Adam Helmy, Essam Berikaa, and Md. Samiul Alam for their endless assistance and encouragement in the lab.

Finally, I would like to thank my family whose support and encouragements kept me going throughout my studies. The example they have set as well as their never-ending stubbornness to understand my research motivated me to continue working towards my goals.

Author contributions

This thesis was written by Santiago Bernal. All the chapters of this thesis represent work completed by me. Yannick D'Mello and Dr. Dan Petrescu contributed to the project frameworks and to the design of the studies.

Table of Contents

List of Figures

List of Tables

List of Acronyms

AFM	Atomic force microscopy
CMOS	Complementary metal-oxide-semiconductor
CQ	Cyclotella Quillensis
DC	Duty cycle
DOS	Density of optical states
DUVL	Deep ultraviolet lithography
EBL	Electron beam lithography
EC	Edge couplers
FAU	Fiber array unit
FDTD	Finite-difference-time-domain
GC	Grating coupler
IL	Insertion loss
MMI	Multi-mode interferometers
PBS	Polarization beam splitters
PhC	Photonic crystals
SEM	Scanning electron microscopy
SiP	Silicon photonics

SNOM	Near-field optical microscopy
SOI	Silicon on insulator
SWG	Subwavelength gratings
TE	Transverse electric
TM	Transverse magnetic

1 Introduction

The ever-growing information and communications technology sector is constantly in need of innovation. The presence of cutting-edge technology in technical fields and in our personal everyday life has created an endless list of applications for optical technologies. In particular, cloud-computing and streaming services have pushed the development and accessibility of high-speed internet. The infrastructure needed to support the demands of today and tomorrow rely heavily on the use of large data centers which require complex communication networks. These networks depend on integrated systems to provide low cost, high efficiency, and small footprint solutions to otherwise very costly or entirely infeasible problems. One way to reach those demands is to use integrated circuit platforms such as silicon photonics (SiP). The main advantage of the SiP platform, aside from the reduced size and cost, is its compatibility with complementary metal-oxide-semiconductor (CMOS) technology which enables it to leverage advanced fabrication techniques. While most Si opto-electronic integrated circuits are built using deep ultraviolet lithography (DUVL), purely passive optical components can be built using electron beam lithography (EBL). This technique allows for relatively short lead times as well as a high lithographic resolution which has enabled the research into subwavelength features used in photonic band engineering.

The continuous search for more sustainable and cheaper solutions has spurred research into the integration of natural and artificial optimization processes into current device designs. These technological advancements are important in order to realize new techniques and develop new components capable of surpassing the otherwise fundamental limitations of current technologies.

1.1 Silicon Photonics

Communications and data exchanged through the internet are hosted by telecommunication networks that rely on electro-optical infrastructure. A growing demand for these services fuels the push for faster transfer speeds and higher bitrates. This need is currently met by optical fiber systems that offer low transmission loss and high bitrates at high propagation speeds [1]. These signals are transmitted at the infrared wavelengths of 1310 nm and 1550 nm, known as the central wavelengths of the O-band and the C-band, respectively. These correspond to the minimum dispersion and loss frequencies in silica optical fibers [2]. The signals in these networks are relayed by transceiver nodes that employ Silicon (Si) - based photonic circuitry.

The Silicon on insulator (SOI) platform is host to a large index contrast between the waveguiding core of silicon (Si) and the surrounding cladding of silicon dioxide (SiO_2). This enables the use of smaller devices and waveguide bends, which leads to more compact and dense optical circuits [3]. SiP integrated circuits can be used to combine thousands of active and passive components. This has led to the research and optimization of active devices such as modulators and photodetectors. However, the indirect bandgap of Si prevents the design of lasers and optical amplifiers. To circumvent this issue, efforts to integrate external laser sources via bonding have taken place. On the other hand, passive components such as grating and edge couplers, polarization beam splitters, and Bragg gratings can be easily fabricated. However, these circuit are limited by their loss. This is mainly due to scattering caused by fabrication imperfections. These defects are primarily due to lithographic smoothing, mask misalignment, and sidewall roughness [4]. Nevertheless, the fabrication limits are regularly tested by the incorporation of subwavelength features into passive SiP designs. These continue to be explored as they can provide larger bandwidths and polarization independence.

1.2 Passive SiP devices

Components that only deal with light are categorized as passive devices, the most basic being a waveguide. Strip waveguides are comprised of a high refractive index core, surrounded by a low index cladding. Light propagates through these waveguides as guided modes. These modes are called transverse electric (TE) or transverse magnetic (TM) depending on the directionality of the electric and magnetic fields inside the waveguide. The mode profile of the two fundamental modes can be seen in Figure 1 for a wavelength of 1550 nm in a typical strip waveguide of 500 nm width and 220 nm height. The fundamental TE mode propagates mainly in the core as it is around 98% confined to the Si. On the other hand, the fundamental TM mode mainly propagates through the cladding as it cannot be confined by the typical 220 nm height of the waveguide.

Figure 1: Mode profile of the fundamental (a) TE and (b) TM modes

Modifying the dimensions of the waveguide allows more modes to propagate. To calculate the number of modes that can propagate in a waveguide, the dispersion relation can be used. These set of equations allow us to quickly find the number of confined modes in a waveguide. The width of the waveguide is most commonly changed to vary the number of confined modes. Suddenly increasing this value can excite higher order modes and lead to multi-mode interferometers

(MMIs) which will be explained in greater detail in chapter 3. On the other hand, reducing this width using a taper will lead to an enlargement in the modal field distribution. This property can be used to design edge couplers (EC) [5].

To couple light into a SiP chip, two techniques can be used. The first involves using an EC where the effective index of the mode needs to be slowly reduced in order to match the mode field diameter of a single mode fiber. EC have a large bandwidth and are largely polarization independent [5]. However, they require very precise alignment and can only be utilized at the edges of the chip, limiting the total number of ECs possible per reticle. Recently, new designs have been introduced to lower the misalignment tolerance by introducing an array of inverse tapers [6]. Additionally, the mismatch in the mode field diameter can be reduced by using subwavelength gratings (SWGs) [7]. An example of an SWG EC can be seen in Figure 2.

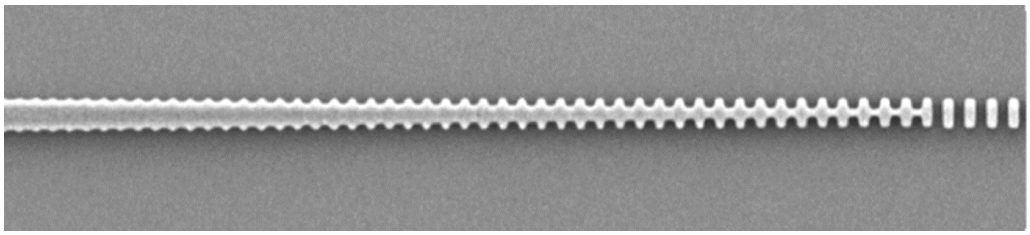

Figure 2: Top view of a SWG EC. Excerpt from [7]

The other way to couple light into a chip is to use a vertical grating coupler (GC). GCs redirect light incident from the top of the chip onto the plane of propagation by modifying the wavevector of the light beam to one supported by the on-chip waveguides [5]. To do so, they employ SWGs in the diffraction regime. The different SWG regimes will be further explained in chapter 2. An example of a GC is shown in Figure 3. GC are advantageous since they can be placed along the surface of the chip, allowing many test structures to be tested. They also boast a higher

misalignment tolerance than ECs. However, GCs have smaller bandwidths and are more sensitive to the polarization of light [5].

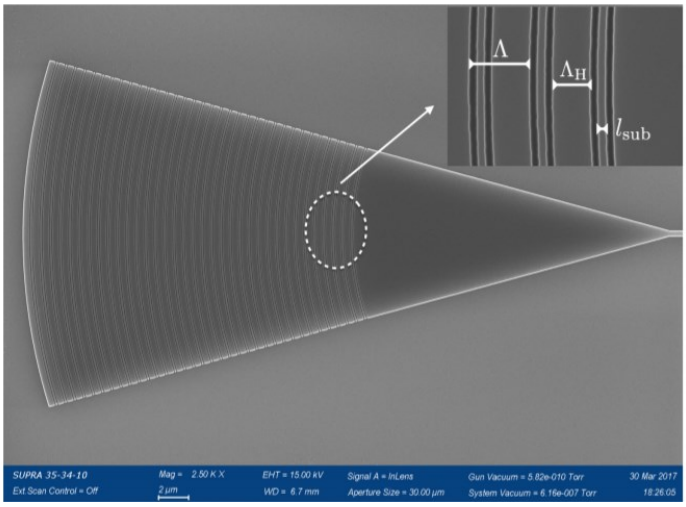

Figure 3: Top view of a SOI grating coupler. Excerpted from [8].

1.3 SiP Fabrication improvements

The introduction of subwavelength features such as photonic crystals (PhC) and SWGs were facilitated by the developments of new fabrication techniques. The two main techniques used in the fabrication of SiP chips are DUVL and EBL.

CMOS-based DUVL is a mature fabrication technique. Its versatility and complexity make it ideal for opto-electronic circuits since it enables the fabrication of devices with metal layers, doping, heating, and multi-etching. It can be used to mass manufacture chips at a low cost. However, the minimum feature size available through DUVL is around 180 nm and the lead times are long [9].

On the other hand, EBL is a newer manufacturing technique mainly used for passive SOI chips. It allows for a high lithographic resolution with a minimum feature size of around 60 nm

and shorter lead times [10]. However, EBL lacks the complexity achievable with DUVL. Nevertheless, these advantages have attracted research into devices with subwavelength features.

1.4 Microscopy techniques

In order to visualize the different new developments made by the fabrication techniques and to understand the structures found in nature, we must use different microscopy techniques. In this thesis, scanning electron microscopy (SEM) was used to measure surface features in the nanoscale, near-field optical microscopy (SNOM) was used to characterize the optical behaviour, and atomic force microscopy (AFM) was used to image the topography of our samples.

1.4.1 Scanning Electron Microscopy

SEM is most commonly used to image nanoscale features of structures. This technique uses an electron beam to image samples in the nanometer scale. The electron beam is focused onto the sample, where they collide. This results in the ejection of backscattered and secondary electrons. These are then detected and converted into an image.

SEM images are often used to validate the fabrication process of SWG and PhC devices in SiP circuits. However, it can also be used to map the elemental composition of samples. This is called electron diffraction spectroscopy. The main advantage of SEM is its imaging speed and the resulting detailed topography. However, it requires that samples be prepared beforehand. Samples with no conductive properties must be coated with a thin conductive film.

In this thesis, SEM measurements were used to image a centric diatom species, to extract dimensions, and to inform the simulation models. The SEM images in this thesis were captured with the help of a technician.

1.4.2 Atomic Force Microscopy

AFM is primarily used to measure the topography of a sample. Each AFM microscope will be equipped with a cantilever, a laser, and a photodiode quadrant. This technique uses a very small cantilever tip that resonates on the surface of the sample due to the atomic forces between them. The surface topography will affect this force and the frequency of oscillation of the tip will change. These movements will be detected using a laser. The laser is aimed at the cantilever and its reflection is captured by the photodiode quadrant. The changes in oscillation frequency will therefore dictate whether the height of the cantilever needs to be adjusted. This height is stored for every point along the sample and a heatmap is generated.

AFM tips are usually only 10 nm to 20 nm wide. This allows for a high level of precision when measuring surface texture and roughness. For AFM, there is no sample preparation needed. However, more precise scans can take a long time. Additionally, the sample can be damaged by the tip in some cases.

In this thesis, AFM measurements were concurrent to the SNOM images and were mainly used to validate the orientation of the diatom shell. This was due to the cantilever tip being larger than the feature sizes found on the sample. The size of the AFM tip was chosen as per the SNOM requirements. The AFM images in this thesis were captured by me.

1.4.3 Scanning Near field Optical Microscopy

Transmission SNOM is used to measure the near-field optical response of a sample. This technique uses a subwavelength aperture at the end of a cantilever to illuminate the sample in the near field. The light is evanescently coupled into the sample at a fixed angle. The distance from the tip to the sample is kept constant using the same technique used by AFM. The light is then

detected via an objective lens beneath. Using this method, it is possible to determine how light propagates through a structure by combining all the scanned points into an image.

The illumination laser used can also be modified to obtain the optical response at different wavelengths. SNOM tips apertures can range from 60 nm to 150 nm. These larger sized tips limit the accuracy of the concurrent AFM image. For SNOM, there is no sample preparation needed, but they must be transparent and relatively thin. Similar to AFM, more precise scans can take a long time and the sample can get damaged. The SNOM also has a lengthy calibration process as both the top and bottom objectives must be properly focused on the same point.

In this thesis, the SNOM images were used to characterize the optical response of the diatom shell. The SNOM tips used had an aperture of 90 nm and a red laser was used to illuminate the sample. The SNOM images in this thesis were captured by me.

1.5 Thesis Objective

In recent years, there has been a growing interest in SWGs and PhCs. Multiple studies have emerged in order to characterize and understand the optical behaviours of these structures in SiP devices and in nature [11-16]. In this thesis, we introduce a potential path to understanding these structures by relying on their optical band diagrams. To do so, we present their use in the design of a SiP low-loss SWG MMI splitter and in the characterization of a centric diatom species. We design and simulate 4 SWG MMIs for both central wavelengths and main polarizations used in SiP. The devices are then fabricated and experimentally validated. Additionally, the optical response of a diatom shell is presented using 3 different microscopy techniques and band structure simulations.

This thesis is divided into 5 chapters. This first chapter provided an overview of the field, and an introduction to passive silicon photonic devices as well as to the different microscopy techniques used in the thesis.

The second chapter covers the theories and principles behind SWG and PhC structures. It also explains the link between the architecture of the devices and their optical behaviour by utilising band structure simulations.

The third chapter introduces the low loss 1x2 SWG MMI splitters. In this section, we discuss the theory and design methodology, the propagation simulations, the experimental results, and the future work for the design.

The fourth chapter goes over the optical response of the Cyclotella Quillensis (CQ) diatoms. It covers their architecture using SEM, their near-field optical response using SNOM and AFM, and their PhC properties using band structure simulations. This work was published in [15].

The fifth chapter summarizes the thesis and provides the next steps needed to expand the work done.

2 Device principles

This chapter will cover the theory and design characteristics of subwavelength structures using band structure simulations and examples from recent literature. We will use simulated band diagrams to explain the relationship between light and its effective environment. We will then apply that theory to 1D and 2D cases by examining the optical behaviour of SWG and PhC, respectively. These concepts will be applied in later chapters to structures found in SiP designs and in nature.

2.1 Band structures

An electro-magnetic wave can be characterized by its spatial and temporal frequencies with $k = \frac{2\pi}{\lambda_0}$ and $\omega = 2\pi f$, respectively, where k is the wavenumber, λ_0 is the frere space wavelength, and f is the frequency. Inside a material, the two are linked by the spectrally dependent refractive index $n(f)$. For example, the refractive index of silicon (Si) for a free-space wavelength (λ_0) of 1550 nm or its equivalent frequency of 193.43 THz is 3.48 [17]. This means that a wave with a λ_0 of 1550 nm in vacuum would get compressed to a λ of 445.4 nm in bulk Si [11]. Any modifications to the material will affect the effective refractive index (n_{eff}) seen by the wave. These geometrical and material modifications lead to devices such as strip and slab waveguides that utilize a high index core surrounded by a low index cladding to confine propagating light. Taking this concept one step further by imposing smaller perturbations in the materials in the order of the reduced wavelength can produce unconventional optical behaviours. Such structures are called PhCs [12, 18-20].

These crystals exist in many forms with different periodic arrangements and dimensions. The dimensionality of a PhC is determined by the angles at which light can interact with the

structure. For example, in a 1D PhC, light only sees a periodic structure if it is travelling in a specific direction (k_x). For a 2D crystal, any wave travelling along a plane (k_x, k_y) will interact with the structure. Finally, in a 3D crystal, an incident photon from any direction (k_x, k_y, k_z) will see the periodicity.

The behaviour of light interacting with such a periodic structure can be described by its photonic band diagram. This diagram represents every combination of frequency and wavevector that can interact with the crystal as points that form curves or bands as seen in Figure 4. Similar to the normalized b-V curves used to determine the number of modes in a waveguide, band diagrams can also be normalized with respect to their lattice constant (a) or pitch (Λ), which is the periodic spacing between the different dielectrics. In other words, crystals designed at microwave frequencies can be also be used at the nanometer scale [21].

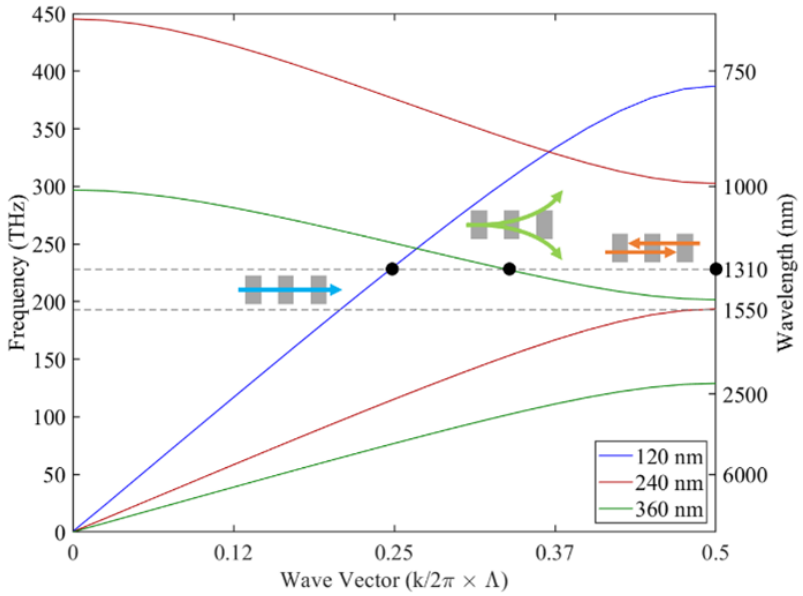

Figure 4: Simulated band structure diagram for an SOI grating with Λ = 120 nm, 240 nm and 360 nm showing the propagation (blue), the reflection (red), and the diffraction (green) regimes.

In these diagrams, the phase velocity (v_p) is represented by the location of a band, while the group velocity (v_g) is represented by the slope at that point [11]. Their values can be found using the following equations, $v_p = \frac{\omega}{k}$ and $v_g = \frac{d\omega}{dk}$.

For SiP devices, the duty cycle (DC) is defined as the ratio of the length of the core material (Si) to the pitch (Λ). The figure above shows the band dependence on the pitch and the three corresponding regimes. For a DC of 0.5 and a large pitch around 360 nm, light with wavelengths in the C-band will radiate from the structure. These bands are not confined to the structure and as such, they will act as lossy modes. These are responsible for diffraction and coupling between the crystal and its surroundings. For a pitch of 240 nm, the same wave will fail to propagate due to the Bragg condition being met. This condition is defined as $\lambda = 2mn_{eff}\Lambda$, where m is an even integer, λ is the wavelength, Λ is the pitch, and n_{eff} is the effective index of the mode. In this regime, forward and backwards scattered waves will destructively interfere creating a region of no propagation, called a band gap. Finally, for a small enough Λ, the wave will propagate in the subwavelength regime. The seemingly constant linear slope of this zone is equivalent to a small dispersion-less region since the group velocity remains relatively constant. This regime will be explained further in the next sections.

These band diagrams in this thesis were simulated using Ansys Lumerical 3D finite-difference-time-domain (FDTD). The PhCs were modeled as infinite planar structures with thickness, t. For SiP devices, t was set to 220 nm, the PhC core to Si, and the cladding to SiO_2. For both materials, the spectral dependency of their refractive index was taken into consideration [22]. In-plane electric and magnetic dipoles were used to excite the TE and TM polarizations, respectively. The in-plane boundary conditions were set as Bloch periodic, while the out-of-plane

boundary conditions were set as perfectly matching layers. Only the first Brillouin zone was simulated following the symmetry points corresponding to the lattice in question and labelled $\Gamma, X, M,$ and K [23]. These symmetry points define the range of all allowed wavevectors that interact with the structure [21]. These simulations allowed us to further understand the design rules when building 1D and 2D PhCs.

2.2 1D crystals: subwavelength gratings

Imposing a 1-dimentional periodicity on a crystal can create an SWG. These structures can be observed in various SiP designs [7, 8, 24-26]. SWGs are composed of a periodic arrangement of two dielectric materials as seen in Figure 5. To alter the optical properties of the structure, the pitch and the DC can be modified.

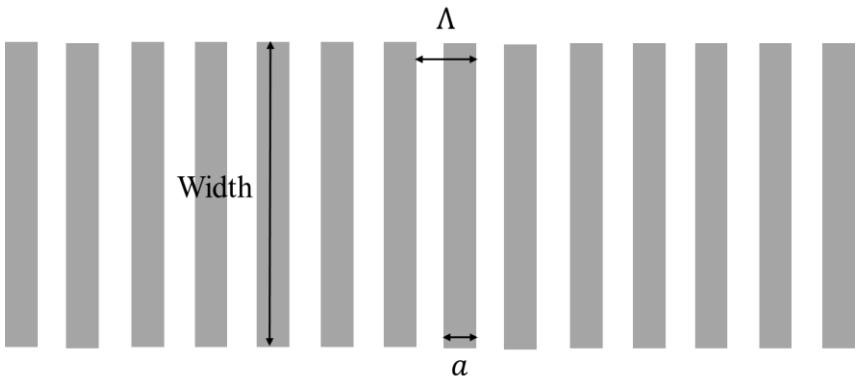

Figure 5: Schematic of a SWG waveguide with relevant parameters.

The subwavelength regime is encountered when the effective wavelength of light is much smaller than the pitch of the grating. In this regime, light propagates through the waveguide as modes travelling though a homogenous material [12]. For this reason, these modes only slightly interact with the discontinuities and the sidewalls roughness of the gratings which allow for low-loss propagation and high fabrication tolerance [24, 27, 28]. This means that an SWG waveguide

can be replaced with an effective material. This can be done following the effective medium theory [29]. To ensure that the SWG waveguide is operating in the SWG regime, the following inequality must hold [12, 30],

$$\Lambda < \frac{\lambda}{2n_{eff}}$$

where n_{eff} is the effective index of the propagating mode. This ensures that the operating bandwidth of the device does not enter the Bragg regime as previously stated. For standard SiP devices operating at 1310 nm and 1550 nm, the largest pitch that supports this condition was found to be around 200 nm [31]. However, in the deep subwavelength region, where $\Lambda \ll \lambda$, an approximation can be used. This approximation follows the Rytov equations [32],

$$n_{\parallel}^2 = \frac{a}{\Lambda} n_1^2 + \left(1 - \frac{a}{\Lambda}\right) n_2^2$$

$$n_{\perp}^{-2} = \frac{a}{\Lambda} n_1^{-2} + \left(1 - \frac{a}{\Lambda}\right) n_2^{-2}$$

where $n_{\parallel}$ is the component of the electric field polarization being parallel to the gratings. Similarly, $n_{\perp}$ is the component of the electric field polarization being perpendicular to the gratings. The physical parameters of the waveguide are represented by a and Λ as the length of each grating and the pitch between them, respectively. The ratio between them is called the duty cycle and is often kept at 0.5 to take advantage of the minimum feature size during fabrication. This means that in most cases, the core (Si) and cladding (SiO_2) contribute equally to the effective index of the SWG structure. The refractive index of the core and cladding materials forming the SWG are represented by n_1 and n_2. In SiP, n_1 and n_2 would be replaced with the refractive index of Si and SiO_2, respectively. For a wave propagating along the SWG, from left to right in the bottom inset of

Figure 6, the effective index of the mode can then be calculated similarly to a strip waveguide with a core refractive index of $n_{\parallel}$. This means that an SWG waveguide will have a lower refractive index compared to a strip waveguide of the same dimensions. This will lead to faster propagations times since the index is inversely proportional to the phase velocity of a mode. This reduced confinement will also affect the two main polarizations differently.

As mentioned in the last chapter, TM modes are not fully confined to the standard SOI strip waveguide. Their lower effective refractive index means that they propagate mainly in the cladding and are not as confined as TE modes. For this reason, TM polarized modes are not as affected by the presence of SWGs in a waveguide [24]. Therefore, the TM modes will have a different band diagram for the same SWG waveguide as can be seen in Figure 6. The position of the TM band is closer to the light line of the cladding as expected. The light line of the cladding is used in band diagrams to determine the cut-off point between confined and lossy modes. It illustrates the border between the diffraction and propagation regimes.

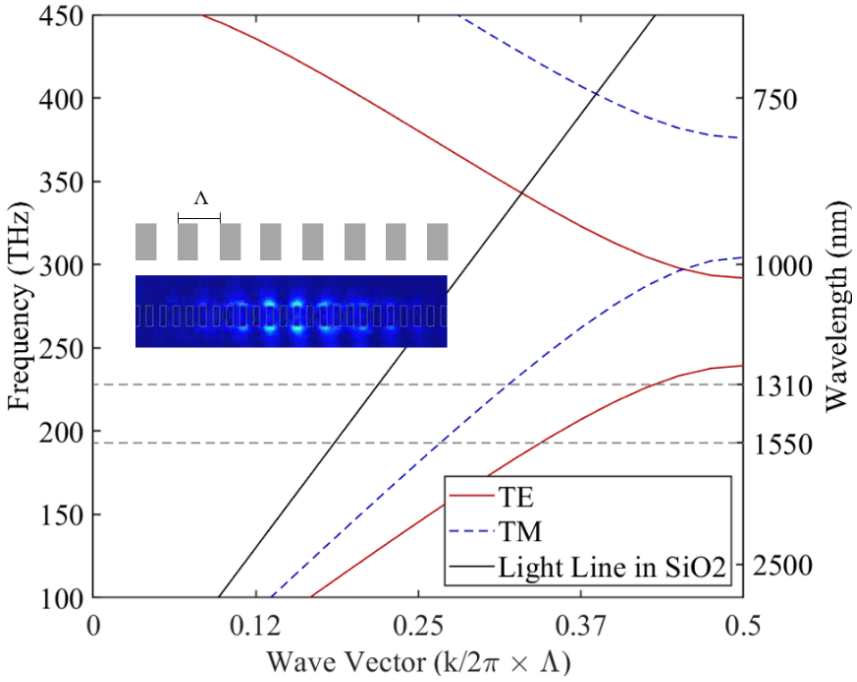

Figure 6: Band diagram, (top inset) schematic, and (bottom inset) propagation simulation of a SWG waveguide. Excerpt from [11].

The parameters of the SWG can be altered for different purposes. For example, fiber to chip devices utilise a larger pitch to access the diffraction regime. In the case of ECs, SWGs can be used to slowly lower the effective index of the mode and therefore decrease its confinement. In the case of GCs, the SWGs are used to form angles of constructive and destructive interference which map out the diffraction orders of the grating [11].

Another advantage of SWGs is the linear sections of the optical bands found in the deep subwavelength regime. These allows for constant group and phase velocities over a large bandwidth covering both the O-band and C-band. This technique can be used to achieve highly broadband performances in waveguides [26], in ECs [25, 31]. These broadband properties have also been used in power splitters as presented in Chapter 3.

2.3 2D crystals: photonic crystals

Increasing the periodicity of a crystal to a second dimension introduces new optical behaviours. PhC structures can be observed in various SiP designs [33, 34] as well as in nature [14, 16]. 2D PhCs are composed of a core material with a periodic arrangement of holes. This lattice of holes can be distributed in a variety of ways, with square and triangular configurations being the most common. Both the spacing between the holes and their individual size can be modified to alter the optical properties of the structure. Figure 7 shows a schematic of a typical square lattice with hole spacing Λ and hole diameter d.

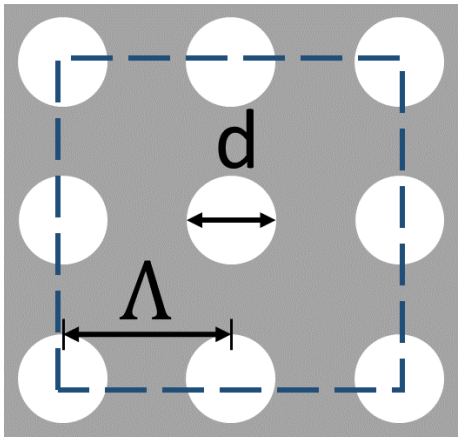

Figure 7: Schematic of a square PhC lattice with relevant parameters.

In SiP designs, PhCs are primarily used due to the presence of a band gap which can be used to either reflect or trap light. Analogous to the energy band gap in semi-conductors, photonic band gaps can be exploited, in this case to manipulate the behaviour of light. For example, adding a defect to the lattice by removing a row or a column of the crystal structure can create a localized mode [18]. This line defect allows light that has a frequency inside the band gap to be confined to the defect and thus propagate through a desired path. While a line defect in a PhC will act as a waveguide, multiple consecutive line defects can cause the emergence of a multi mode waveguide

[35]. Unlike conventional symmetric dielectric waveguides or step-index waveguides that rely on total internal reflection with a high index core and a low index cladding, PhC waveguides can guide light by surrounding the waveguide with a PhC whose band gap aligns with the frequency of the propagating light. The main advantage of PhC waveguides is their low propagation loss in sharp turns. This is due to the mode being unable to propagate inside the PhC, forcing it to remain confined to the line defect. However, their discrete lengths can impose issues when designing devices with specific lengths, such as MMIs [35].

Photonic band gaps are also used to reflect light. As such, the difference in refractive index between TE and TM modes can be exploited in devices such as polarization beam splitters (PBS) that utilize PhCs [36-38]. Due to the birefringent nature of SiP, it is possible to design PhCs with different behaviours for different polarizations. The band diagram in Figure 8 demonstrates this difference between the two orthogonal polarizations inside of a crystal with a triangular lattice. The introduction of a polarization sensitive PhC inside a MMI allows for loss-less propagation for TM modes, while TE modes get reflected. In these designs, The TE modes would get collected as back-reflections while the TM modes would get collected at their mirrored self-imaging length. These devices allow for a high extinction ratio due to the large separation between the two output ports.

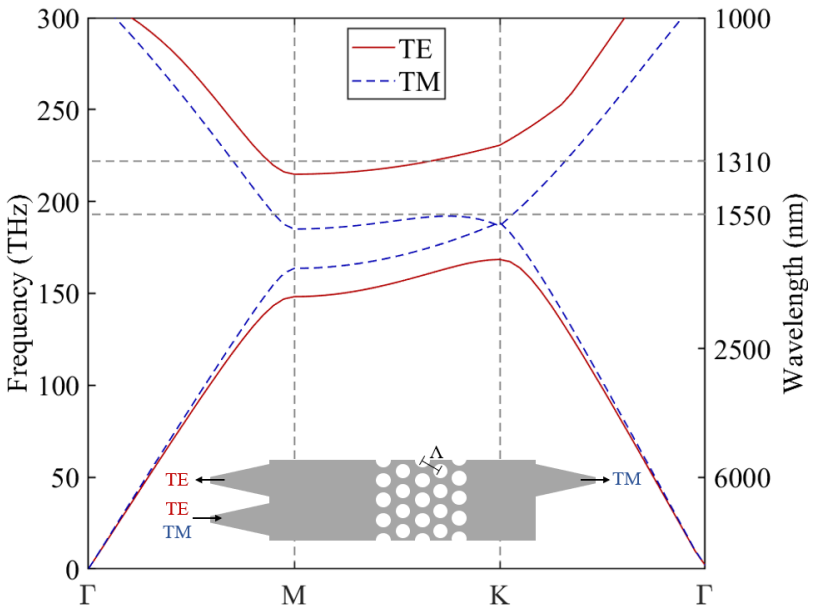

Figure 8: Band diagram of a photonic crystal used in the design of an MMI functioning as a polarization splitter. Excerpt from [11].

In nature, PhCs can be seen used due to the presence of a collapsed band gap, also known as a pseudo gap. These pseudo gaps are represented by a set of parallel bands with negligible spacing between them that can occur when the difference in refractive index of the core and cladding is small. Additionally, these bands can also occur when the PhC has small hole diameters compared to the spacing between them. The exact location of these collapsed bandgaps is determined by the lattice configuration, the lattice spacing, and the refractive index mismatch between the two dielectrics. These pseudo gaps represent frequencies of slow light since the slope of the parallel bands is often reduced. This behaviour is believed to aid coupling as it supports a higher density of optical states (DOS) [14, 15]. This optical property of PhCs will be further examined in Chapter 4.

3 SWG MMI 3-dB splitters

In this chapter, we present the design, fabrication, and testing of 3-dB splitters using a SWG MMIs. The devices were designed to operate in both the C-band and O-band for TE and TM polarizations. An optimization process was then undertaken to minimize the insertion loss (IL) of 4 different devices spanning the combinations of the two polarizations and central wavelengths previously stated. Some specifications will be omitted from this chapter since they are under intellectual property protection.

3.1 Introduction

The refractive index contrast between Si and the surrounding glass cladding (SiO_2) as well as the low loss in the SiP platform facilitates high optical confinement and subsequently denser circuits. These integrated circuits have placed demands on power splitters to be more compact, efficient, and broadband. Power splitters from part of the building block for many photonic devices such as switches, modulators, and multiplexers. They can either have equal or variable power splitting capabilities.

There are various approaches used in SiP to create a power splitter. One approach is to use directional couplers. These can be compact and different splitting ratios can be achieved [4]. However, they have narrow bandwidths and low fabrication tolerance [39]. To solve this issue, adiabatic directional couplers can be used. These devices have a larger bandwidth, but also need a much larger footprint [40]. Another approach is to use MMI-based designs since these have large bandwidths and are more tolerant to fabrication variations. Recently, SWG features have been used in these designs to reduce their footprint and to further increase their bandwidth [41].

3.2 Design

Multimode waveguides form a type of optical passive device known as MMIs which are characterized by their number of input and output ports. MMIs can have multiple single mode waveguides as inputs and outputs denoted by N and M respectively such that the device can be named a N × M MMI. This drastic change in waveguide width excites higher order modes of which each propagates with its own propagation constant $\beta = k_0 n_{eff}$, where n_{eff} is the effective index of each mode in the waveguide and k_0 is the wavenumber $2\pi/\lambda_0$. As these modes propagate through the multimode waveguide and interfere with each other, they produce self-images of the input field. The location of these self images is highly depended on the beat length (L_π) of the two lowest order modes [42] as,

$$L_\pi = \frac{\pi}{\beta_0 - \beta_1} \approx \frac{4 n_{eff} W_e^2}{3\lambda_0}$$

where W_e is the effective width of the MMI region considering the Goos-Hahnchen shift. This shift can be thought of as varying the penetration depth of the mode into the low index cladding. However, in high-contrast waveguides, this extra depth can be ignored so that the width of the waveguide will equal its effective width. The field distribution in at any length L along the MMI can therefore be expressed as the sum of all the guided modes,

$$\Psi(y, L) = \sum_{V=0}^{m-1} c_V \varphi_V(y) \exp\left[j \frac{V(V+2)\pi}{3L_\pi} L\right]$$

where V is the mode number, c_V is the field excitation coefficient, $\varphi_V(y)$ is the modal field distribution of each mode, and L is the length along the MMI. The self-images can then be calculated as $L_{si} = p(3L_\pi)$, where p can be any even or odd integer to produce direct replicas or

mirrored images of the input field, respectively [42]. Multiple images of the input field can also be obtained at distances $L_{si,N} = \frac{p}{N}(3L_\pi)$, where N is the number of images symmetrically spaced within the width of the MMI. For example, the first two-fold image can be found at a length of $L = (3L_\pi)/2$. This location is commonly used to design 3-dB intensity splitters.

The addition of the SWG regime into the design above affects the n_{eff} of the propagating modes. By reducing the overall effective index of the structure, the resulting beat length is reduced which results in shorter values of L_{SI} and therefore in shorter overall MMI device lengths [43]. Furthermore, the SWG regime also offers extended bandwidths since it almost removes the strong frequency dependence of the effective refractive index and allows for a shorter difference between TE and TM beat lengths [44]. Using these concepts, 4 low-loss intensity splitters SWG 1x2 MMIs were designed. The device schematic seen in Figure 9 illustrates the different parameters used.

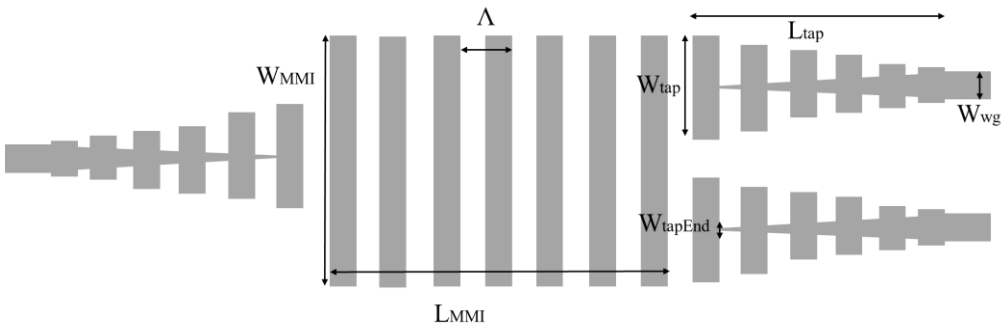

Figure 9: Schematic of the SWG MMI with relevant parameters.

The pitch, Λ, was chosen to ensure the device operated in the subwavelength regime as per its band diagram and to remain within the fabrication minimum feature size limits. The taper length, L_{taper}, was optimized through simulations to minimize loss. The thickness and width of the input and output waveguides, w_{wg}, were set to 220 nm and 500 nm, respectively.

A conventional MMI requires enough width to support a multitude of modes at the cost of increasing the self-imaging length for both TE and TM modes. This would consequently increase the overall footprint. Hence, the MMI width, w_{MMI}, was set to 3 μm to introduce multimode interferometry for both polarizations at a short self-imaging length. The MMI length, L_{MMI}, was then chosen to collect the first folded self-image and optimized through simulation to improve the collection of both TE and TM light at the output ports. The width of the input and output ports were also tapered to minimize the insertion loss of the device and to slowly convert the refractive index of the mode from a bulk strip waveguide to a SWG waveguide. They were parameterized using the width of the waveguide at the multimode waveguide, w_{tap}, and the width of the bulk to SWG waveguide taper, w_{tapEnd}. Finally, the DC was maintained at 0.5 to maximize the feature sizes available through fabrication.

3.3 Simulations

Band diagram and wave propagation simulations were done using Ansys Lumerical 3D FDTD to optimize the device. The band structure calculations were performed similarly to those explained in chapter 2.1. Propagation simulations were used to extract the IL, the bandwidth, and the imbalance from the device. The simulations were performed over the C-band and O-band separately to reduce the computation time. A source object was placed at the input port and two power monitors were placed at each of the output ports. All the boundary conditions of the simulation were set to perfectly matched layers to avoid them interfering with the device.

The parameters used were chosen based on the device designs and their fabrication viability. In order to optimize the device for each wavelength and polarization, the following parameters were modified: $L_{MMI}, W_{tap}, L_{tap}$. The following parameters were kept constant

throughout the four designs: $w_{mmi}, w_{tapEnd}, w_{wg}$. The optimization was done by varying each parameter individually and selecting the device with the lowest insertion loss.

Different pitch values were simulated with the intention of challenging the fabrication limits while also ensure its feasibility. The lower value was picked as $\Lambda = 175$ nm, which would result in a minimum feature size of 87.5 nm. This would ensure its fabrication under EBL but would limit its implementation in circuits built using DUVL. For this reason, the second pitch value chosen was $\Lambda = 200$ nm. The band diagrams in Figure 10 illustrate the difference between the two Λ.

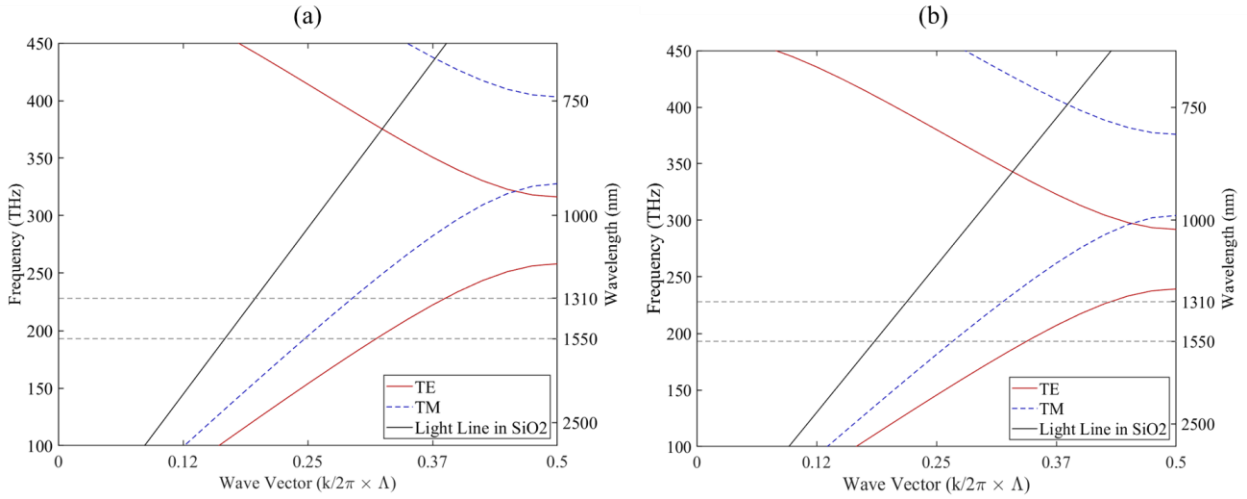

Figure 10: Simulated band diagram of the SWG MMI for a pitch of (a) 175 nm and (b) 200 nm

The length of the MMI was restricted by the discrete nature of SWGs. It was set as $\Lambda * n$, where n is the number of gratings needed to achieve the desired length. For example, an SWG MMI operating at 1550 nm with a period of 170 nm and a width of 3 μm would have a self-imaging length of 3.325 μm. This would correspond to a n value of 19.56. Therefore, the device was simulated for using an n parameter of 19 and 20 and the resulting best IL was selected.

The width and length of the tapers were also optimized. The three tapers used were kept identical in each device order to maintain the reciprocity of light through the device, allowing the SWG MMI to function as a splitter or as a combiner depending on the input/output ports used. The length of the tapers was long enough to allow for a slow effective index transition for the input modes travelling along a strip waveguide into the SWG MMI. It follows that for longer tapers, the gradual transition would lead to smaller losses, however, that would be against the objective of making a compact device. A balance between taper length and loss was therefore achieved for tapers of 8 to 9.3 μm.

The width of the tapers determined the number of higher order modes that could be excited inside the MMI and therefore the location of the self-images. Their larger size also allowed for some tolerance in the exact location of collecting the self-image. This tolerance was needed due the exact MMI length needed being unobtainable using SWGs as previously stated. The table below summarizes the parameters that varied between each of the 4 devices designed.

Table 1: Relevant parameters used in the SWG MMIs.

Wavelength	Polarization	Pitch	MMI Length	Taper Length	Taper Width
1310 nm	TE	175 nm / 200 nm	3.50 μm	8 μm	1.3 μm
1550 nm	TE	175 nm / 200 nm	3.33 μm	8 μm	1.4 μm
1310 nm	TM	175 nm / 200 nm	8.05 μm	8.5 μm	1.45 μm
1550 nm	TM	175 nm / 200 nm	6.30 μm	9.3 μm	1.5 μm

The entire devices were simulated including the SWG structures, the tapers and the bulk strip waveguides at the input/output ports. The electric field profile of the devices can be seen in Figure 11. The total length of the device was calculated as $2 * L_{tap} + L_{MMI}$. This resulted in a footprint of 19.5 µm × 3 µm for the TE case, and 24.9 µm × 3 µm for the TM case.

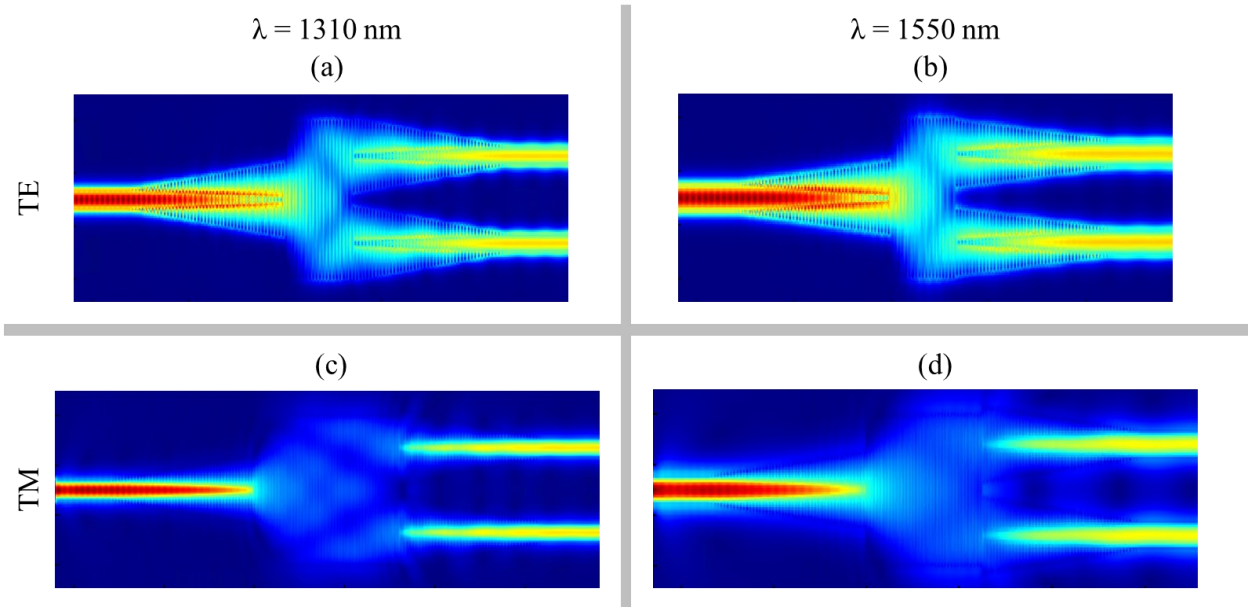

Figure 11: Field-profile propagation through the 4 SWG MMIs for the TE (a-b) and a TM (c-d) modes at 1310 nm and 1550 nm.

The loss was extracted from the two power monitors placed at the upper and lower ports on the output of the device. The transmission, T, from these monitors was then converted to the IL as per the following equations,

$$T = \frac{P_{out}}{P_{in}}$$

$$IL(\text{dB}) = -10 \log_{10} \frac{P_{out1} + P_{out2}}{P_{in}}$$

where P_{in} is the input power, P_{out} is the power at the monitor(s). The TE simulated devices demonstrated a minimum loss of 3.10 dB and 3.11 dB at 1310 nm and 1550 nm, respectively which is 0.09 dB and 0.10 dB lower than the target imposed by the required 3.01 dB splitting ratio. On the other hand, the TM devices resulted in a simulated IL of 0.46 dB and 0.63 dB for the middle wavelength of the O-band and C-band, respectively. The absorption loss from the materials were not considered for these simulations. The loss profile of the 4 devices can be seen in Figure 12.

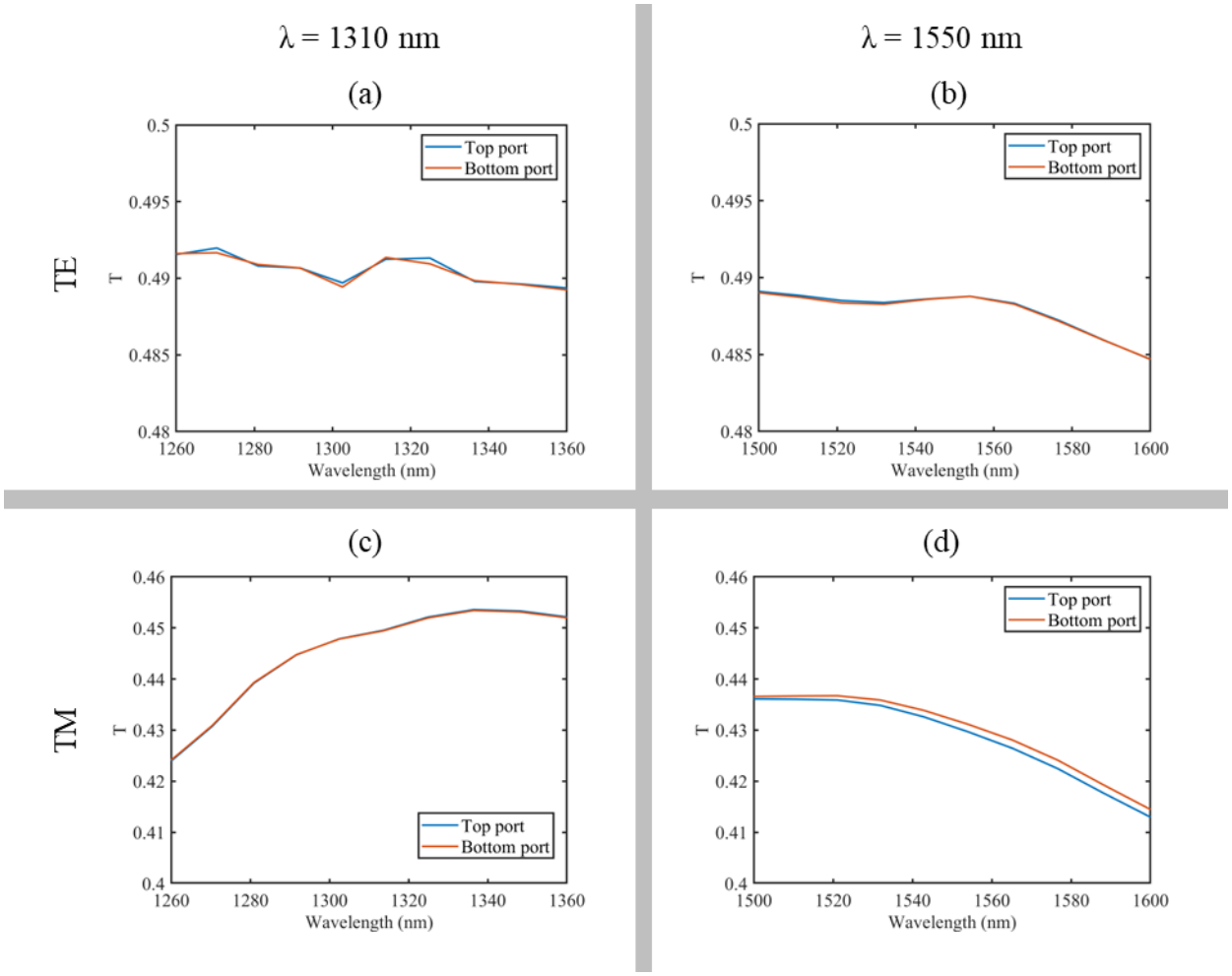

Figure 12: Simulated IL at the output ports of the SWG MMIs for the TE (a-b) and TM (c-d) modes over the C and O-bands.

The maximum imbalance simulated was found to be negligible for both TE and TM modes. The bandwidth of the device was not fully simulated to reduce optimization time. However, the entire O-band and C-band are comprised as targeted, and the full bandwidth is over 100 nm. The independent analysis of the O-band and C-band was driven by the equipment in the lab. Due to the limitations in our experimental setup, only the wavelengths ranging from 1260 nm to 1360 nm and from 1500 nm to 1600 nm could be tested.

3.4 Experimental results

The proposed MMI splitters were fabricated on a SOI wafer with 220 nm top silicon thickness, a buried oxide (BOX) layer, and an oxide cladding at AIM photonics Inc. In order to test the devices, multiple variations were made using 4 test structure circuits. The IL of the device was found using circuits with a back-to-back configuration and a targeted IL of around 1 dB and 10 dB. These optical circuits were comprised of 2 GCs and 10 to 100 TE devices. Additional circuits were fabricated to test the imbalance of the devices, the IL of the GC used and to align the testing equipment. To test the imbalance, circuits with individual devices were made. These utilized 3 GCs, one for the input and two for the outputs. To test the IL of the GCs, circuits comprised of 2 back-to-back GCs were used. An example of the layout of the 4 circuits can be seen in Figure 13. The layout submitted for fabrication consisted of 40 test structures and 10 alignment circuits.

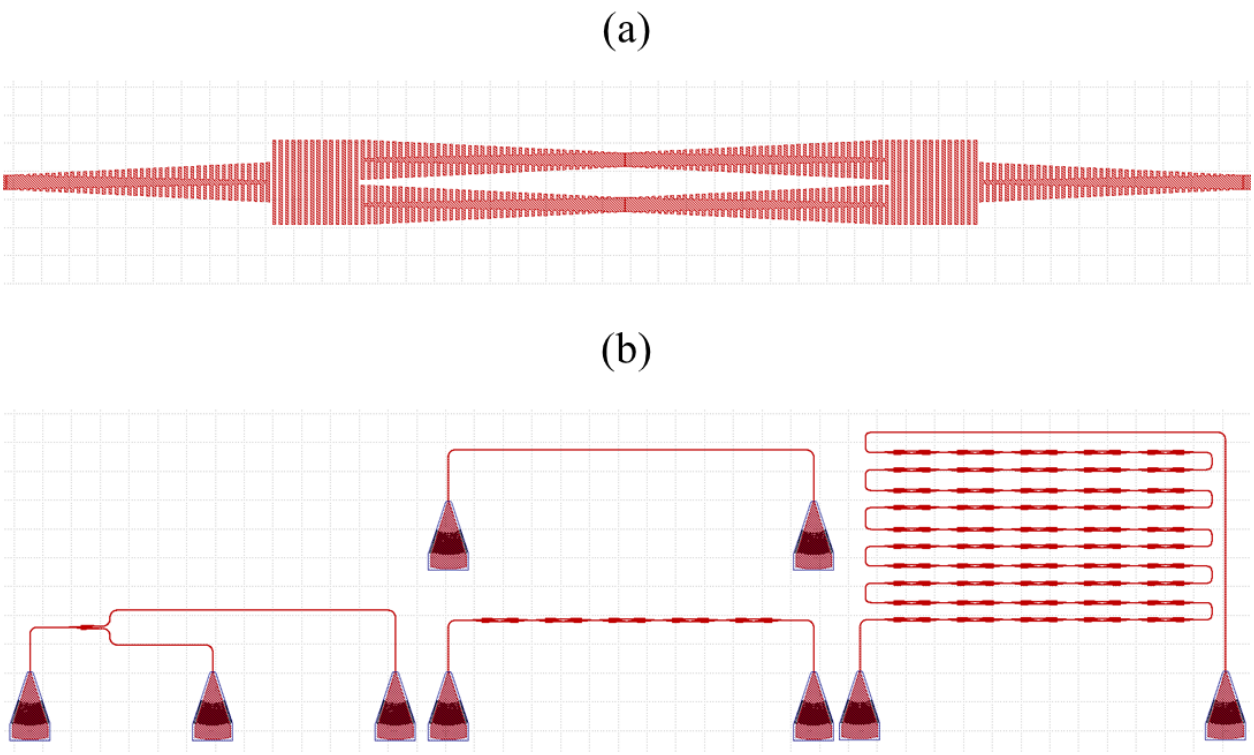

Figure 13: Layout of the SWG MMI showing the (a) back-to-back test structure and the (b) 4 circuits used in for each variation.

The fabricated chip was tested using an automated setup. This setup consists of a fiber array unit (FAU), two Yenista TUNICS T100s-HP C-band and O-band tunable lasers, a Yenista CT400 Passive Optical Component Tester, and a polarization controller. The setup was also capable of heating the chip and of doing electrical measurements, however those functionalities were not used. A picture of the setup is shown in Figure 14.

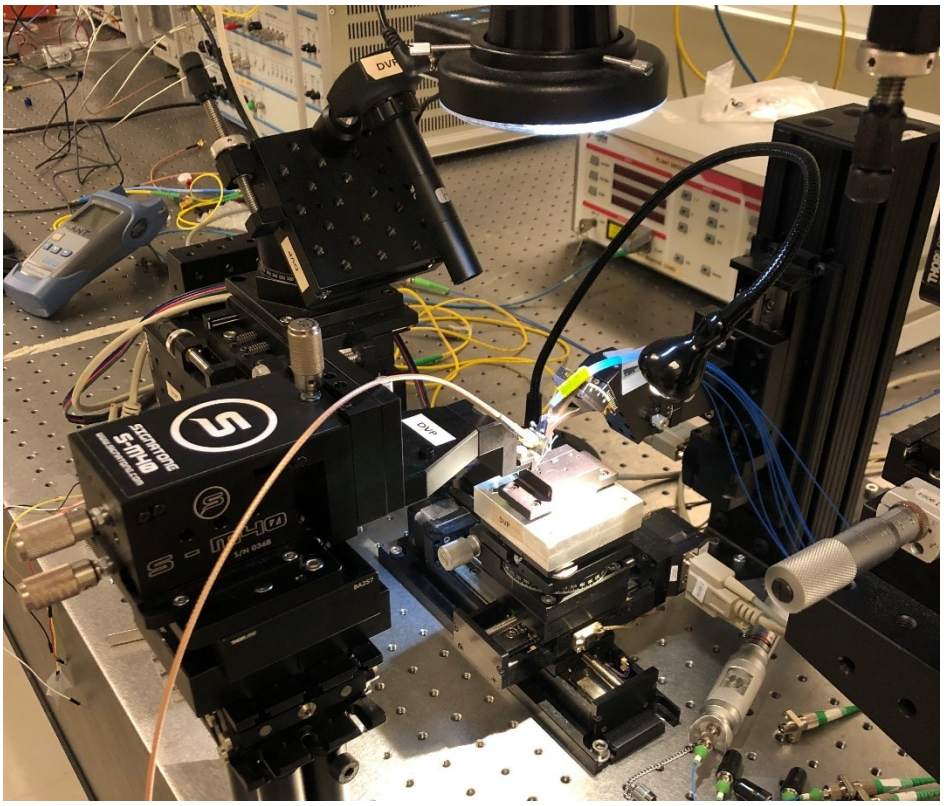

Figure 14: Automated setup used for measurements

The followings steps are needed to test passive devices using this setup. Initially, the FAU must be aligned to the chip. To do so, we adjust the pitch, yaw, and roll of the FAU with the alignment circuits. Since the GCs used are optimized at 1550 nm or 1310 nm, the angle of the FAU can be adjusted until the peak IL of the back-to-back GC circuit is centered at the desired wavelength. The polarization controller is then used to ensure the correct polarization is being coupled to the chip. To do so, the peak IL is again minimized. A typical transmission spectrum for a GC is shown in Figure 15. Since the wavelength sensitivity of the GC is quite high, it must be calibrated out from future measurements. The equipment used allowed up to 4 signals to be measured simultaneously using the 4 input ports of the CT400. This allowed us to test the different test structures without having to change the connections of the FAU. The power measured by these 4 ports can be seen in the raw measurement data plotted below.

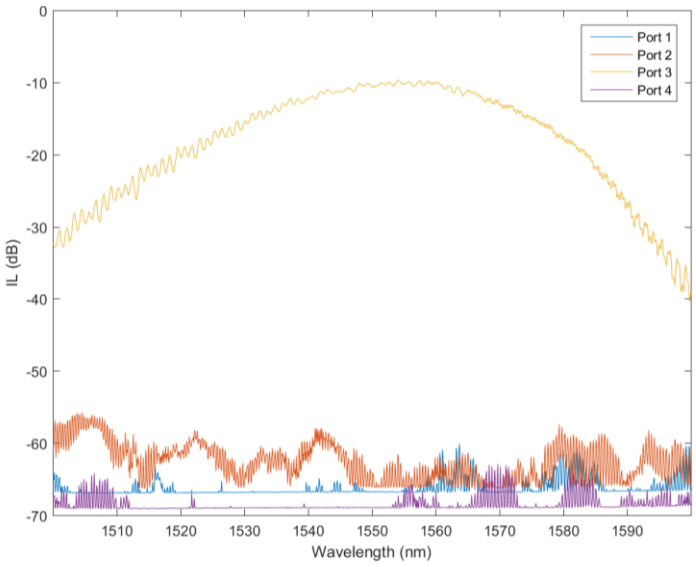

Figure 15: Transmission spectrum of back-to-back GCs

Once the FAU has been aligned to the chip and the correct polarization is set, the IL of each test structure can be measured. The best raw measurements for the single device circuit are shown in Figure 16 for both the O-band and C-band TE SWG MMIs.

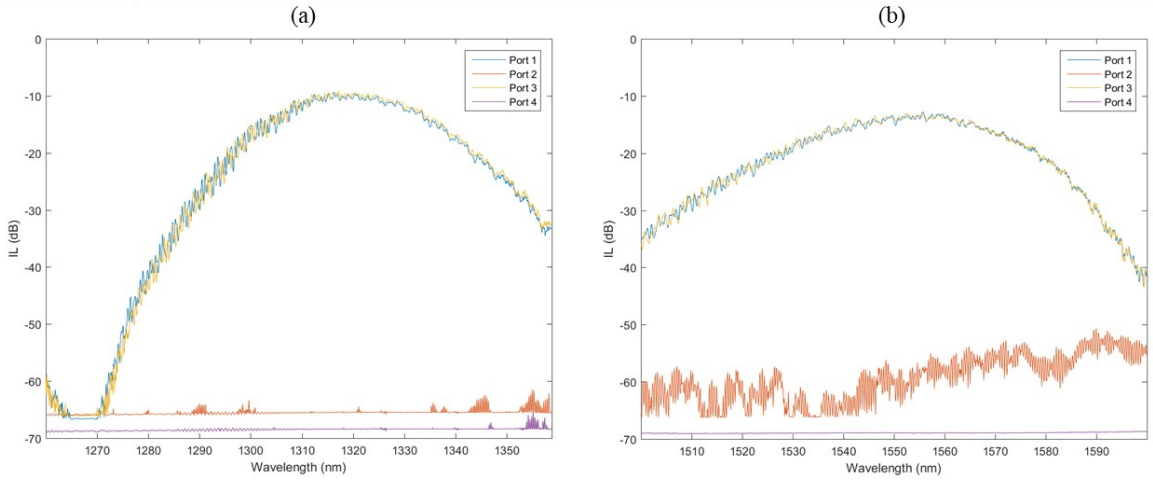

Figure 16: Measured IL of TE SWG MMI devices in the (a) O-band and (b) C-band

These plots closely follow the typical GC response due to the large bandwidth of the devices. The narrowband response of the TE O-band GCs used meant that the device's response

could not be extracted properly as some of the signal was lost to the noise floor of the measuring equipment. Nevertheless, the IL could still be extracted for the central wavelength. In order to extract the IL of the individual device, the back-to-back GC response (in dB) is subtracted from the raw measurement. Additionally, a rolling average was used to remove the noise coming from any small polarization or coupling misalignments. The calibrated IL is shown in Figure 17.

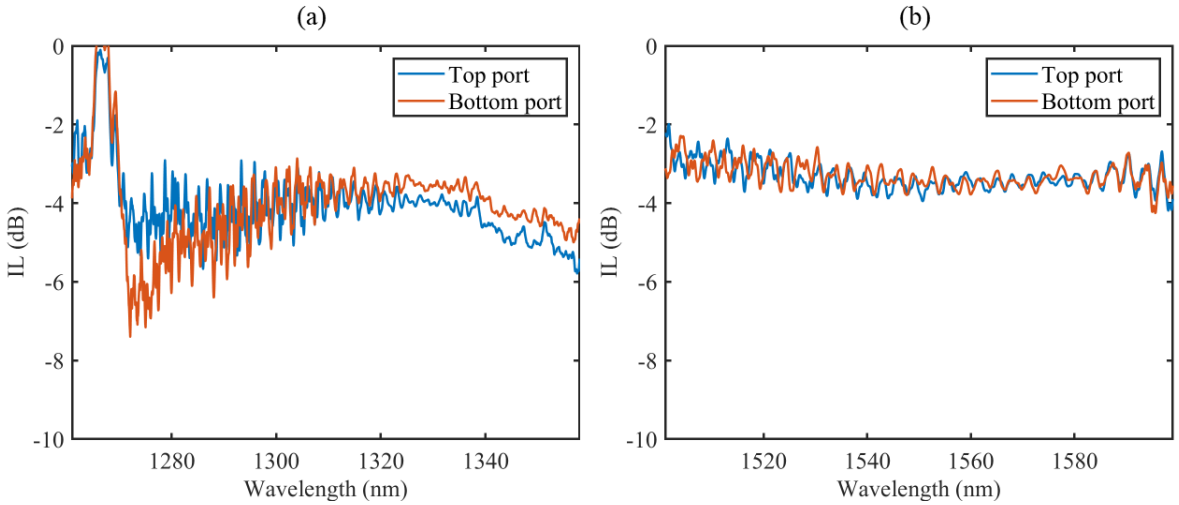

Figure 17: Calibrated IL from TE SWG MMI devices in the (a) O-band and (b) C-band

After the largely wavelength dependent transmission of the grating couplers was removed, the IL was measured to be 1.25 dB and 0.85 dB for the TE with a pitch of $\Lambda = 175$ nm at 1310 nm and 1550 nm, respectively. The maximum experimental imbalance between the two output ports is around 1.18 dB and 0.91 dB for the O-band and C-band variations. The IL for TE devices with a pitch of $\Lambda = 200$ nm at 1310 nm and 1550 nm was 0.54 dB and 0.96 dB, respectively. The maximum experimental imbalance between the two output ports is around 1.09 dB and 0.73 dB for the O-band and C-band variations. Across all the 40 test structures, the average IL for TE devices were 1.21 dB and 1.29 dB at 1310 nm and 1550 nm, respectively. The standard variation was 0.49 for the O-band and 0.65 for the C-band.

3.5 Discussion and Future work

The experimental results suggest that a larger pitch leads to lower losses. However, this is due to the fabrication limits and not to the device performance. The smaller pitch slightly violated the design rules imposed by the foundry and therefore, it was expected that it could contain fabrication errors. These errors include missing an SWG and effectively doubling the pitch for certain sections of the MMI. This leads to a difference in the effective refractive index seen by the propagating modes and therefore a change in the location of the self-image.

The experimental values are also different from the simulated values since the fabrication uncertainties will effectively change some of the device parameters such as the exact pitch, the width of the MMI, the shape of the tapers and the location of the output and input ports. Additionally, the grating coupler alignment plays a big factor in the insertion loss value and in the bandwidth of the device. The full bandwidth of the device was not properly measured since the experiments were only done in the range of the grating couplers used. However, the targeted relatively flat response across 100 nm was achieved. Another reason the IL was higher than simulated could be because of the layout. As the device is relatively small in width, both output ports are close to each other, and this could cause a weak coupling effect between them before they are separated in the layout. The absorption of Si and SiO_2 would also add losses which were not considered during simulations.

Our results improve on the design of previous SWG MMI splitters by having a low experimentally demonstrated IL. In [41], the IL was simulated to 0.5 dB at 1550 nm while the experimental IL was not reported. Our device also has a smaller footprint compared to the reported 24 μm by 3 μm in [41]. Devices with loss as low as 0.085 dB have been shown in [45], however the bandwidth was limited to the C-band. Ultracompact devices such as the splitter presented in

[46] have demonstrated IL less than 0.1 dB across both the C-band and O-band while maintaining a small footprint.

The above designs could be improved by decreasing its IL further, bypassing the fabrication limits, and increasing its functionality to output different splitting ratios. The IL could be reduced further by adding more spacing between the two output ports and ensuring there is no coupling effects between them. The minimum feature size imposed by the fabrication limits could be circumvented by introducing a tilt to the SWG. Tilting the SWG provides an additional parameter that can be optimised. This angle effectively reduces the pitch of the device by decreasing the horizontal distance between the two dielectrics [47]. This creates an effective pitch which can be calculated as $\Lambda * sec\theta$, where θ is the tilt angle. These structures have already been used to produce a broadband PBS [44]. Additionally, asymmetric MMI designs have been shown to produce varying splitting ratios by adding a cut to one of the sides [41, 48]. These three improvements could be combined to create a low-loss, polarization independent, asymmetric power splitter.

3.6 Conclusion

The concepts of multimode interference and birefringence engineering in subwavelength gratings were employed in the design of 4 low-loss intensity splitters. Device simulations demonstrated a broadband response over 100 nm in the telecommunications C-band and O-band for both TE and TM modes. The effective insertion loss was simulated to be less than 0.1 dB and 0.63 dB for TE and TM modes, respectively. However, the experimental results revealed a higher IL due to the fabrication and measurements inaccuracies. These results motivate further research into tilted SWG structures that allow for more precise refractive index engineering. By adding an angle to the gratings, the structure can be interpreted as a 2D PhC lattice. This results in the addition

of another parameter to adjust the effective index of both TE and TM modes by introducing an effective pitch without the need to wait for fabrication methods with smaller feature sizes.

4 Optical response of centric diatoms

This chapter covers the use of 2D PhC found in nature. More specifically, the shell of the centric diatom species known as Cyclotella Quillensis (CQ) was examined. Its optical behaviour was investigated using different microscopy techniques and band structure simulations [15].

4.1 Introduction

Solar energy is one of the highest potential sources for renewable energy. This is because the amount of sunlight that travels to the surface of the Earth in one hour is enough to satisfy the world's yearly power consumption [49]. However, this potential is not being fulfilled since only around 1.8% of the world's power is currently being produced using solar energy [50, 51]. This is partially due to the low efficiency and high costs of solar panels. There is therefore an opportunity for a new technology to enhance the absorption efficiency of solar panel farms. To this effect, researchers have turned to plants who also orient themselves towards the sun to capture as much sunlight as possible.

Natural systems already take advantage of this energy through photosynthesis. This process is estimated to absorb as much as 8 times the energy requirements of our society today [52]. Most of this can be attributed to unicellular phytoplankton found in most bodies of water. These organisms are called diatoms and they are responsible for over 25% of the global supply of oxygen [53]. They are also play a major role in the ocean carbon cycle with a 40% contribution [54]. Diatoms are subjected to constant turbulences and lack any mobility. This means that they cannot orient themselves or maintain an acquired orientation towards the sun like terrestrial plants. However, they still inhabit almost all bodies of water. Their abundance has made it clear that understanding their optical behaviour could lead to developments in energy harvesting and carbon sequestration.

Diatoms grow a glass-like shell called a frustule by assimilating silica from surrounding waters. This structure provides protection, chemical buffering, and light manipulation [55]. Frustules are unique to each diatom species, of which there are over 100,000 variations [56]. Despite this, they share enough similarities to be categorized into two physical groups based on their symmetry. Diatom frustules can be sorted as centric or pennate depending on their radial or bilateral symmetries, respectively [56]. Frustules are comprised of two parts: valves, and girdles. The symmetric valves are attached by the girdle as seen in Figure 18. Additionally, frustules often display a periodic arrangement of holes resembling a PhC [55]. It is speculated that the appearance of this PhC through millions of years of evolution was to aid the photosynthetic process. The lack of mobility of diatoms suggests that their shell evolved to capture incident light irrespective of orientation or that they possess extremely efficient photosynthetic conversion mechanisms. However, diatoms mainly utilize common photosynthetic pigments such as chlorophyll A [57]. Therefore, multiple studies have been done on the optical and overall behaviour of the frustule in order to understand their role in the proliferation of diatoms [13, 14, 58-60].

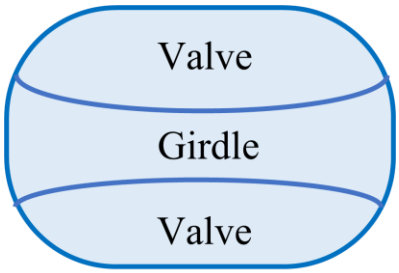

Figure 18: Schematic of a typical frustule

Our work examines the frustule of CQ, a centric diatom species, through simulations and experimental findings. By utilizing SEM, SNOM, AFM, and band diagrams, we are able to model and visualize the role of the frustule.

4.2 Frustule architecture

The architecture of the frustule was obtained from 14 SEM images using an FEI Quanta 450 FE-ESEM. The diatom cells were obtained from the Culture Collection of Algae at the University of Texas at Austin (UTEX). They were then grown until enough samples could be collected. They were also cleaned using a mixture of sulphuric acid and hydrogen peroxide (piranha). This step was necessary to obtain highly resolved images of the frustule without any organic mater. Finally, the samples had to be coated with a 5-10 nm layer of either Al or Pt to be compatible with the SEM.

The images of CQ valves revealed the presence of two sections. The outer section was comprised of multiple symmetrically undulated rows of holes, while the inner section was mostly flat. The center of the valve contained a few randomly distributed perforations known as fultoportula. On the other hand, the exterior of the valve exhibited a mostly square PhC with holes of 100 $\pm$ 30 nm in diameter and spaced 250 $\pm$ 50 nm apart. The valves, and consequently the CQ diatoms, ranged from 10 to 50 µm in diameter. The girdle was mostly smooth and had a height of 5 $\pm$ 1 µm. The entire architecture of the silica shell can be seen in Figure 19.

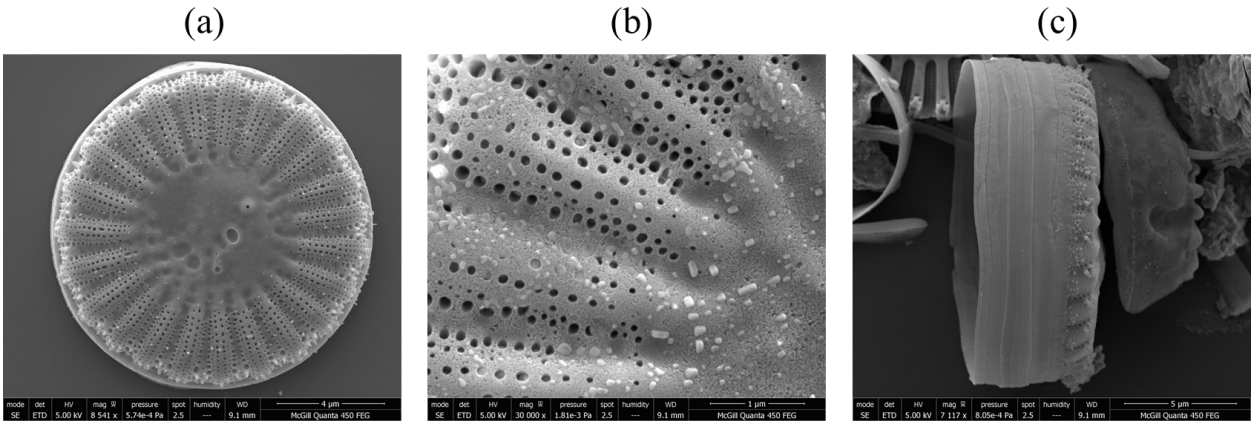

Figure 19: SEM images of CQ showing the (a) top view and (b) square PhC lattice of the valve, and (c) side view of the girdle.

4.3 Experimental results

SNOM and concurrent AFM measurements were performed using a WITec Alpha 300S microscope. Cleaned samples were deposited on a cover slip and imaged. To do so, a silicon tip with an aperture of 90 nm was put on the microscope cantilever. This aperture size was chosen to match the hole dimensions of the valve. The SNOM imaging was done at a wavelength of 660 nm using a Thorlabs LP660-SF60. This wavelength was chosen to match one of the absorption peaks of chlorophyll A. This laser diode was operated by an LDM9LP laser mount connected to an LDC ITC 4001 controller. The SNOM and AFM setup can be seen in Figure 20.

(a) (b)

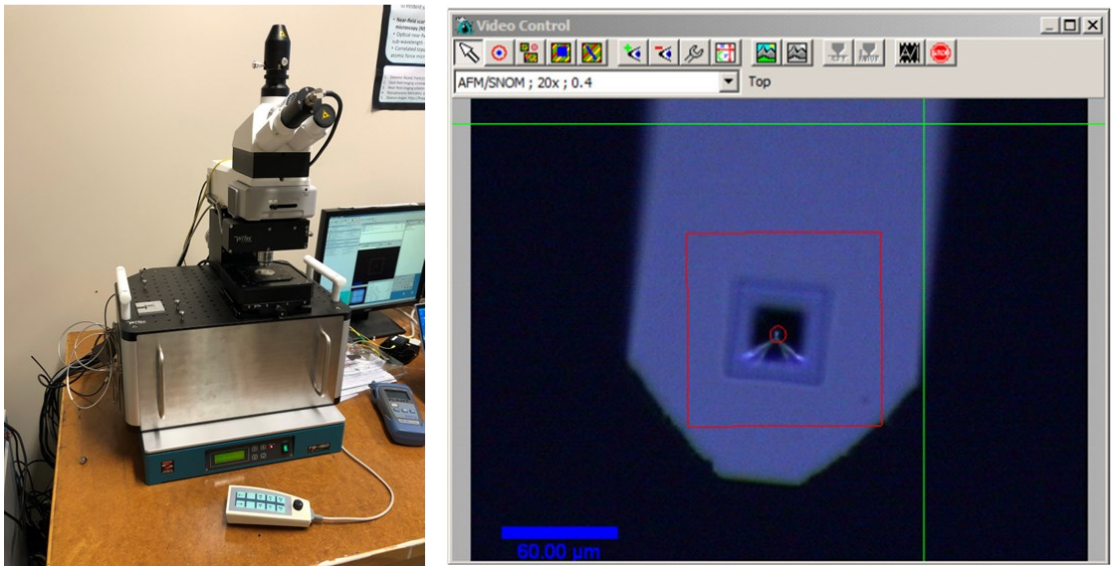

Figure 20: (a) SNOM and AFM setup and (b) the cantilever used as seen from top lens of the instrument

The SNOM and concurrent AFM measurements were done on the exterior of a CQ valve as can be seen in Figure 21. At each position, the aperture coupled light in the near-field to the sample and the bottom lens collected it in the far-field. Additionally, the relative height of the sample was measured by the AFM which allowed us to reference it with the topography observed

in SEM images. In this way, the AFM and SEM images complemented each other. However, the limitations of the instrument were highlighted by the blurred regions of the AFM image as the cantilever struggled to reach the areas of high curvature.

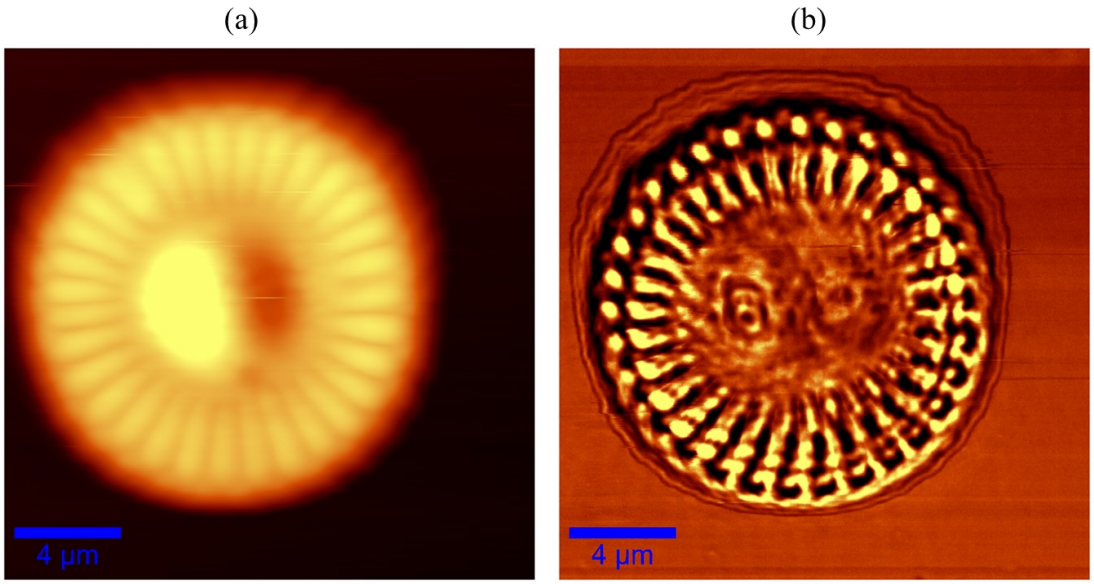

Figure 21: (a) AFM topography and its corresponding (b) SNOM image

The dark zones with respect to the monochrome background in the SNOM image represent regions of scattered light. On the other hand, the bright areas correspond to high transmission intensities. The radial continuity of the bright zone along the outer section of the valve demonstrated light propagation toward the center or the edges and ultimately into the girdle. This waveguiding property was verified using band structure simulations.

4.4 Band structure simulations

Band diagram simulations were done using Ansys Lumerical 3D FDTD. The band structure calculations were performed similarly to those explained in chapter 2.1. The core material was set as silica to represent the frustule and the hole material as water to represent the environment of CQ diatoms. The lattice spacing and hole diameter were taken from the SEM images as $\Lambda = 250$

nm and $d = 100$ nm. The lattice configuration was estimated as square. The resulting band diagram can be seen in Figure 22.

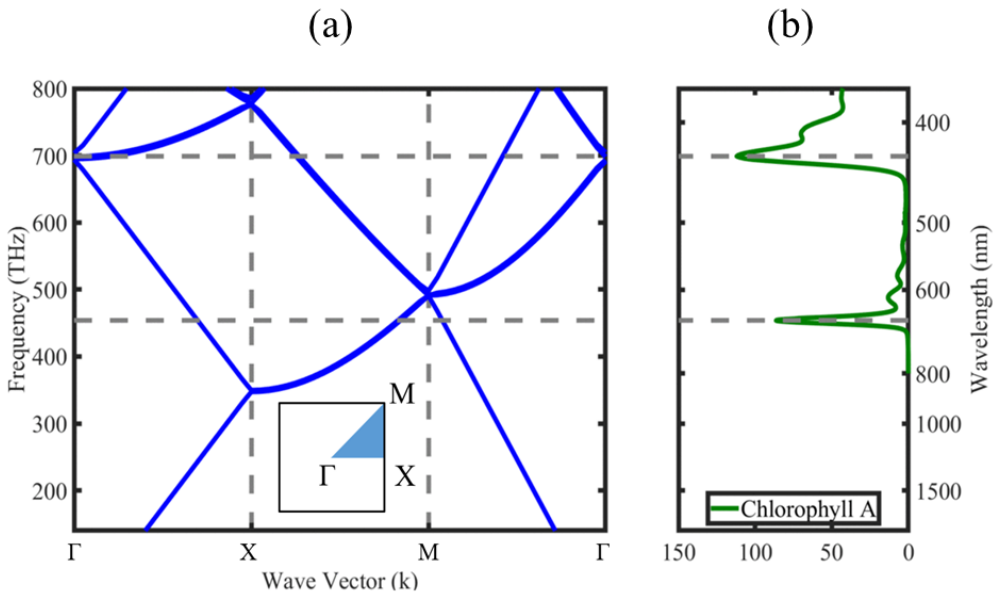

Figure 22: (a) Band diagram of a square PhC in relation to (b) the absorption spectrum of chlorophyll A.

The band diagram revealed the presence of pesudogaps at the peak absorption wavelengths of chlorophyll A [61]. The gap between bands was negligible due to the small hole diameters and low index contrast of the PhC. These collapsed band gaps represented frequencies that propagated with a reduced group velocity and remained confined to the frustule for longer [11]. The two adjacent, parallel bands between the X-M symmetries and 600-850 nm were therefore indicative of waveguiding. Additionally, the 4 modes at the Γ point and 450 nm represented a very high density of states. This high density of optical states facilitated the coupling of light to the frustule due to the availability of multiple wavevectors.

4.5 Discussion and Future work

The experimental results revealed the presence of waveguiding within the valve and diffraction at the intersection between the valve and the girdle. The bright radial lines in the SNOM images coincided with the location of the PhCs on the valve and the band diagrams confirmed the presence of guided modes. The band diagram simulations also illustrated the high DOS at the peak absorption wavelengths of chlorophyll A. These results suggest 3 optical mechanisms exhibited by the frustule. These are light harvesting, distribution, and retention.

The larger surface area of the valve alongside the coupling efficiency of the PhCs would allow the frustule to harvest sunlight. The waveguiding properties of the PhCs along the valve exterior would then diffract light radially into the girdle. The dark edges of the valve in the SNOM images suggests that light coupled into the girdle would get redirected and could remain trapped. This supports the use of the girdle to guide and circulate light as proposed in [60]. The girdle would therefore act as a racetrack resonator which would confine light until it was ready to be absorbed by the chloroplasts. The retention would need to be long enough to compensate for the absorption rate of chloroplasts during periods of varying illumination. Validating these assumptions would reinforce the theory that the frustule evolved over millions of years in order to adapt to its environment and to ensure the survival of diatoms.

The above speculations could be improved by expanding the simulation and experiments to the individual components. A racetrack propagation simulation of the girdle would confirm its waveguiding properties while also identifying its retention rate or Q factor. The coupling efficiency of the valve could be simulated or experimentally found by using two optical fibers. The waveguiding properties of the valve could be explored by performing a higher resolution SNOM. A more accurate band diagram calculation could also be achieved by considering the

random perturbations in the lattice. These would effectively smear the band structure. As a result, a larger range of wavelengths could be adapted by each band. This would also increase the range of the high DOS which would allow for a larger coupling bandwidth.

4.6 Conclusion

Centric diatoms such as CQ grow a glass-like shell composed of a quasi-periodic arrangement of holes forming a PhC. Its optical properties were analysed using SEM, SNOM, AFM and 3D FDTD simulations. Our experimental work illustrated the optical response of different sections of the frustule. The SEM images revealed the architecture of the structure while the SNOM and concurrent AFM images illustrated the waveguiding properties of its exterior. A photonic band structure simulation complemented the experiments by indicating the location of pseudogaps at the peak absorption wavelengths of chlorophyll A. These results support the theory that diatom frustules have evolved to harvest, retain, and redistribute light in order to aid the photosynthetic process.

5 Conclusion

5.1 Summary

The ever-growing need for more sustainable and efficient technologies has motived the interest into SiP and nature designs using SWGs and PhCs. The compatibility of SiP with the mature CMOS fabrication flow has made it a viable solution for low-cost, mass manufacturing integrated photonic circuits. However, there is a constant need to introduce devices with lower energy consumptions, higher bandwidths, and new functionalities. In this thesis, we introduced a potential path to solve these issues by relying on novel designs that push the fabrication limits and that are inspired by the longest running optimization process, evolution.

In chapter 2, we gave an overview of the design principles of SWGs and PhCs using their optical band structures. We presented different crystals structures and explained their optical behaviour by linking it to their band structures. We provided recent examples of SiP devices utilizing the different band diagrams regimes, mainly propagation, reflection, and diffraction.

In chapter 3, we presented 4 low-loss SWG MMI splitters for the optical C-band and O-band, and the TE and TM polarizations. Our study challenged the fabrications limits and utilized the deep SWG regime to achieve bandwidths of over 100 nm. The best IL of the devices was experimentally found to be 0.54 dB, which was higher than the simulated value. The maximum imbalance tested was 1.18 dB.

In chapter 4, we presented the optical response of the centric diatom species known as CQ. Through different microscopy techniques and band structure simulations, we speculate that their shell not only acts as a protective shield, but also aids photosynthesis. We established the links between SNOM, AFM, and SEM images. Additionally, these experimental results complemented

the band diagram of the frustule which revealed pseudogaps at the peak absorption wavelengths of chlorophyll A, the most common pigment found in diatoms. This work was published in [15].

5.2 Future work

The future work for each project presented in this thesis was highlighted in chapters 3.5 and 4.5. These involve achieving polarization independence in SiP, completely understanding how the different mechanism within diatom shells interact with their environment and each other and integrating natural and artificial optimization processes into SiP.

The Si layer thickness on-chip is typically limited at 220 nm, which is smaller than the approximately 500 nm required to confine a fundamental mode in the C-band. This difference in its cross-section combined with a high index contrast induces an effective birefringence in SiP devices. It implies that fundamental modes corresponding to the TE and TM polarizations confined in the waveguide experience different effective indices as they propagate through the SiP waveguides. This polarization dependence reduces their applicability in photonics circuits mainly due to a larger overall footprint on-chip, increased fabrication costs and an eventually lower feasibility when being deployed in the telecommunications infrastructure. This difference is most apparent when comparing the minimum bend radius needed for sharp on chip turns in waveguides. For example, TM modes require around a 30 μm turn radius at 1550 nm to ensure that the loss is less than 0.1% while TE have similar losses for only around a 10 μm bend radius [4]. This highlights the need for polarization independent devices in SiP. One way to achieve this in SWG MMIs is to add a tilt to the gratings. This additional parameter allows us to reduce the effective pitch of the device and to modify the refractive index in the parallel and perpendicular directions differently [43]. This would translate to different beat lengths for TE and TM modes and as such, polarization independent MMI devices can be created.

A deeper study into the individual contributions of the frustule sections to photosynthesis would lead to a complete understanding of the optical properties of diatoms. This investigation would examine the 3 optical mechanisms believed to be used by the frustule. The disordered lattice configuration could lead to more efficient light harvesting by increasing the DOS in the diffraction regime. The waveguiding properties of the valve and the girdle could lead to light efficiently being redistributed as needed. Finally, the retention of the girdle acting as a racetrack resonator could compensate for the conversion rate of chloroplasts during periods of varying illumination. Ultimately, the complete understanding of these mechanisms could lead to their integration into SiP devices. This approach could lead to the sudden emergence of new device functionalities in nanophotonics. This integration of natural designs could be analogous to the current integration of computer aided designs, which has already produced promising new devices such as ultra-compact splitters using artificial intelligence [62, 63]. However, unlike the sudden introduction of computer aided designs, the use of natural systems would require a more complete understanding of their optical behaviour.

6 References

[1] T. G. Brown, "Optical fibers and fiber-optic communications," *Fiber optics handbook,* 2002.

[2] A. Yariv and P. Yeh, *Photonics: optical electronics in modern communications*. Oxford university press, 2007.

[3] R. Soref and J. Larenzo, "All-silicon active and passive guided-wave components for λ= 1.3 and 1.6 μm," *IEEE Journal of Quantum Electronics,* vol. 22, no. 6, pp. 873-879, 1986.

[4] L. Chrostowski and M. Hochberg, *Silicon photonics design: from devices to systems*. Cambridge University Press, 2015.

[5] R. Marchetti, C. Lacava, L. Carroll, K. Gradkowski, and P. Minzioni, "Coupling strategies for silicon photonics integrated chips," *Photonics Research,* vol. 7, no. 2, pp. 201-239, 2019.

[6] E. Berikaa, S. Bernal, Y. D'Mello, D. Mao, and D. V. Plant, "Misalignment-Tolerant Ultra-Broadband Edge Coupler Based on 10 Inverse Tapers," in *2021 Photonics North (PN)*, 2021: IEEE, pp. 1-1.

[7] P. Cheben, J. H. Schmid, S. Wang, D.-X. Xu, M. Vachon, S. Janz, J. Lapointe, Y. Painchaud, and M.-J. Picard, "Broadband polarization independent nanophotonic coupler for silicon waveguides with ultra-high efficiency," *Optics Express,* vol. 23, no. 17, pp. 22553-22563, 2015/08/24 2015, doi: 10.1364/OE.23.022553.

[8] Y. Wang, L. Xu, A. Kumar, Y. D'Mello, D. Patel, Z. Xing, R. Li, M. G. Saber, E. El-Fiky, and D. V. Plant, "Compact single-etched sub-wavelength grating couplers for O-band application," *Optics Express,* vol. 25, no. 24, pp. 30582-30590, 2017/11/27 2017, doi: 10.1364/OE.25.030582.

[9] S. Pauliac, S. Landis, J. Foucher, J. Thiault, and O. Faynot, "Hybrid lithography process for nano-scale devices," *Microelectronic engineering,* vol. 83, no. 4-9, pp. 1761-1766, 2006.

[10] L. Chrostowski, H. Shoman, M. Hammood, H. Yun, J. Jhoja, E. Luan, S. Lin, A. Mistry, D. Witt, and N. A. Jaeger, "Silicon photonic circuit design using rapid prototyping foundry process design kits," *IEEE Journal of Selected Topics in Quantum Electronics,* vol. 25, no. 5, pp. 1-26, 2019.

[11] Y. D'Mello, O. Reshef, S. Bernal, E. El-fiky, Y. Wang, M. Jacques, and D. V. Plant, "Integration of periodic, sub-wavelength structures in silicon-on-insulator photonic device design," *IET Optoelectronics,* vol. 14, no. 3, pp. 125-135, 2020.

[12] R. Halir, P. J. Bock, P. Cheben, A. Ortega-Moñux, C. Alonso-Ramos, J. H. Schmid, J. Lapointe, D.-X. Xu, J. G. Wangüemert-Pérez, Í. Molina-Fernández, and S. Janz, "Waveguide sub-wavelength structures: a review of principles and applications," *Laser & Photonics Reviews,* vol. 9, no. 1, pp. 25-49, 2015, doi: https://doi.org/10.1002/lpor.201400083.

[13] Y. D'Mello, D. Petrescu, J. Skoric, M. Campbell, M. Andrews, and D. Plant, "Characterization of the photonic response in nitzschia filiformis phytoplankton," in *CLEO: QELS_Fundamental Science*, 2018: Optical Society of America, p. JTh2A. 96.

[14] Y. D'Mello, S. Bernal, J. Skoric, D. Petrescu, M. Andrews, and D. V. Plant, "Photonic crystal behavior of nitzschia filiformis phytoplankton for chlorophyll a photosynthesis," in *CLEO: QELS_Fundamental Science*, 2019: Optical Society of America, p. JW2A. 121.

[15] S. Bernal, Y. D'Mello, D. Petrescu, M. Andrews, and D. V. Plant, "Optical Response of the Centric Valve in Cyclotella Quillensis Diatoms," in *CLEO: Applications and Technology*, 2020: Optical Society of America, p. JW2A. 1.

[16] A. R. Parker and H. E. Townley, "Biomimetics of photonic nanostructures," (in eng), *Nat Nanotechnol,* vol. 2, no. 6, pp. 347-53, Jun 2007, doi: 10.1038/nnano.2007.152.

[17] H. H. Li, "Refractive index of silicon and germanium and its wavelength and temperature derivatives," *Journal of Physical and Chemical Reference Data,* vol. 9, no. 3, pp. 561-658, 1980, doi: 10.1063/1.555624.

[18] J. D. Joannopoulos, P. R. Villeneuve, and S. Fan, "Photonic crystals: putting a new twist on light," *Nature,* vol. 386, no. 6621, pp. 143-149, 1997/03/01 1997, doi: 10.1038/386143a0.

[19] I. Staude and J. Schilling, "Metamaterial-inspired silicon nanophotonics," *Nature Photonics,* vol. 11, no. 5, pp. 274-284, 2017/05/01 2017, doi: 10.1038/nphoton.2017.39.

[20] P. Cheben, R. Halir, J. H. Schmid, H. A. Atwater, and D. R. Smith, "Subwavelength integrated photonics," *Nature,* vol. 560, no. 7720, pp. 565-572, 2018/08/01 2018, doi: 10.1038/s41586-018-0421-7.

[21] J. D. Joannopoulos, P. R. Villeneuve, and S. Fan, "Photonic crystals: putting a new twist on light," *Nature,* vol. 386, pp. 143-149, 1997.

[22] E. D. Palik, *Handbook of optical constants of solids*. Academic press, 1998.

[23] J. D. Joannopoulos, S. G. Johnson, J. N. Winn, and R. D. Meade, "Molding the flow of light," *Princeton Univ. Press, Princeton, NJ [ua],* 2008.

[24] P. J. Bock, P. Cheben, J. H. Schmid, J. Lapointe, A. Delâge, S. Janz, G. C. Aers, D.-X. Xu, A. Densmore, and T. J. Hall, "Subwavelength grating periodic structures in silicon-on-insulator: a new type of microphotonic waveguide," *Optics express,* vol. 18, no. 19, pp. 20251-20262, 2010.

[25] P. Cheben, D. Xu, S. Janz, and A. Densmore, "Subwavelength waveguide grating for mode conversion and light coupling in integrated optics," *Optics express,* vol. 14, no. 11, pp. 4695-4702, 2006.

[26] Z. Ruan, L. Shen, S. Zheng, and J. Wang, "Subwavelength grating slot (SWGS) waveguide on silicon platform," *Optics express,* vol. 25, no. 15, pp. 18250-18264, 2017.

[27] M. Zadka, U. D. Dave, and M. Lipson, "High tolerance of metamaterial waveguides to fabrication variations," in *CLEO: Science and Innovations*, 2019: Optical Society of America, p. SF1J. 7.

[28] A. Rizzo, U. Dave, A. Freitas, S. P. Roberts, A. Novick, M. Lipson, and K. Bergman, "Fabrication-Robust Silicon Photonics Platform in Standard 220 nm Silicon Processes," in *2021 IEEE 17th International Conference on Group IV Photonics (GFP)*, 7-10 Dec. 2021 2021, pp. 1-2, doi: 10.1109/GFP51802.2021.9674005.

[29] S. Berthier and J. Lafait, "Effective medium theory: Mathematical determination of the physical solution for the dielectric constant," *Optics Communications,* vol. 33, no. 3, pp. 303-306, 1980.

[30] A. Maese-Novo, R. Halir, S. Romero-García, D. Pérez-Galacho, L. Zavargo-Peche, A. Ortega-Moñux, I. Molina-Fernández, J. Wangüemert-Pérez, and P. Cheben, "Wavelength independent multimode interference coupler," *Optics express,* vol. 21, no. 6, pp. 7033-7040, 2013.

[31] M. Papes, P. Cheben, D. Benedikovic, J. H. Schmid, J. Pond, R. Halir, A. Ortega-Moñux, G. Wangüemert-Pérez, N. Y. Winnie, and D.-X. Xu, "Fiber-chip edge coupler with large mode size for silicon photonic wire waveguides," *Optics express,* vol. 24, no. 5, pp. 5026-5038, 2016.

[32] S. Rytov, "Electromagnetic properties of a finely stratified medium," *Soviet Physics JEPT,* vol. 2, pp. 466-475, 1956.

[33] L. Xu, D. Mao, J. Zhang, Y. Wang, Z. Xing, M. S. Alam, M. Jacques, Y. D'Mello, S. Bernal, and D. V. Plant, "Broadband Polarization Beam Splitters Based on MMI Couplers with Internal Photonic Crystals Fabricated Using 193 nm Photolithography," in *2021 Optical Fiber Communications Conference and Exhibition (OFC)*, 2021: IEEE, pp. 1-3.

[34] C. Wang, C.-Z. Zhou, and Z.-Y. Li, "On-chip optical diode based on silicon photonic crystal heterojunctions," *Optics express,* vol. 19, no. 27, pp. 26948-26955, 2011.

[35] H.-J. Kim, I. Park, O. Beom-Hoan, S.-G. Park, E.-H. Lee, and S.-G. Lee, "Self-imaging phenomena in multi-mode photonic crystal line-defect waveguides: application to wavelength de-multiplexing," *Optics express,* vol. 12, no. 23, pp. 5625-5633, 2004.

[36] Y. Shi, D. Dai, and S. He, "Proposal for an ultracompact polarization-beam splitter based on a photonic-crystal-assisted multimode interference coupler," *IEEE Photonics Technology Letters,* vol. 19, no. 11, pp. 825-827, 2007.

[37] Y. Shi, N. Shahid, M. Li, A. Berrier, S. He, and S. Anand, "Experimental demonstration of an ultracompact polarization beamsplitter based on a multimode interference coupler with internal photonic crystals," *Optical Engineering,* vol. 49, no. 6, p. 060503, 2010.

[38] L. Xu, Y. Wang, E. El-Fiky, D. Mao, A. Kumar, Z. Xing, M. G. Saber, M. Jacques, and D. V. Plant, "Compact broadband polarization beam splitter based on multimode interference coupler with internal photonic crystal for the SOI platform," *Journal of Lightwave Technology,* vol. 37, no. 4, pp. 1231-1240, 2019.

[39] Z. Lu, D. Celo, P. Dumais, E. Bernier, and L. Chrostowski, "Comparison of photonic 2× 2 3-dB couplers for 220 nm silicon-on-insulator platforms," in *2015 IEEE 12th International Conference on Group IV Photonics (GFP)*, 2015: IEEE, pp. 57-58.

[40] Y. Wang, L. Xu, H. Yun, M. Ma, A. Kumar, E. El-Fiky, R. Li, N. Abadíacalvo, L. Chrostowski, N. A. F. Jaeger, and D. V. Plant, "Polarization-Independent Mode-Evolution-

Based Coupler for the Silicon-on-Insulator Platform," *IEEE Photonics Journal,* vol. 10, no. 3, pp. 1-10, 2018, doi: 10.1109/JPHOT.2018.2835767.

[41] E. El-Fiky, Y. D'Mello, Y. Wang, J. Skoric, M. G. Saber, A. Kumar, A. Samani, L. Xu, R. Li, and D. Patel, "Ultra-broadband and compact asymmetrical beam splitter enabled by angled sub-wavelength grating MMI," in *CLEO: Science and Innovations*, 2018: Optical Society of America, p. STh4A. 7.

[42] L. B. Soldano and E. C. Pennings, "Optical multi-mode interference devices based on self-imaging: principles and applications," *Journal of lightwave technology,* vol. 13, no. 4, pp. 615-627, 1995.

[43] R. Halir, P. Cheben, J. M. Luque-González, J. D. Sarmiento-Merenguel, J. H. Schmid, G. Wangüemert-Pérez, D. X. Xu, S. Wang, A. Ortega-Moñux, and Í. Molina-Fernández, "Ultra-broadband nanophotonic beamsplitter using an anisotropic sub-wavelength metamaterial," *Laser & Photonics Reviews,* vol. 10, no. 6, pp. 1039-1046, 2016.

[44] A. Herrero-Bermello, J. M. Luque-González, A. V. Velasco, A. Ortega-Monux, P. Cheben, and R. Halir, "Design of a broadband polarization splitter based on anisotropy-engineered tilted subwavelength gratings," *IEEE Photonics Journal,* vol. 11, no. 3, pp. 1-8, 2019.

[45] N. Yang and J. Xiao, "A compact silicon-based polarization-independent power splitter using a three-guide directional coupler with subwavelength gratings," *Optics Communications,* vol. 459, p. 125095, 2020/03/15/ 2020, doi: https://doi.org/10.1016/j.optcom.2019.125095.

[46] J. Xiao and Z. Guo, "Ultracompact Polarization-Insensitive Power Splitter Using Subwavelength Gratings," *IEEE Photonics Technology Letters,* vol. 30, no. 6, pp. 529-532, 2018, doi: 10.1109/LPT.2018.2801337.

[47] A. Herrero-Bermello, J. M. Luque-Gonzàlez, R. Halir, P. Cheben, A. Ortega-Moñux, I. Molina-Fernández, and A. V. Velasco, "Zero-birefringence silicon waveguides based on tilted subwavelength metamaterials," *IEEE Photonics Journal,* vol. 11, no. 5, pp. 1-8, 2019.

[48] A. Zanzi, A. Brimont, A. Griol, P. Sanchis, and J. Marti, "Compact and low-loss asymmetrical multimode interference splitter for power monitoring applications," *Optics letters,* vol. 41, no. 2, pp. 227-229, 2016.

[49] L. R. Brown, *The great transition: Shifting from fossil fuels to solar and wind energy*. WW Norton & Company, 2015.

[50] E. Wesoff, "IEA: Global installed PV capacity leaps to 303 gigawatts," ed: Greentechmedia, 2017.

[51] A. Jäger-Waldau, "Snapshot of photovoltaics− March 2021," *EPJ Photovoltaics,* vol. 12, p. 2, 2021.

[52] U. Steger, W. Achterberg, K. Blok, H. Bode, W. Frenz, M. Kost, C. Gather, G. Hanekamp, R. Kurz, and D. Imboden, *Sustainable development and innovation in the energy sector*. Springer Science & Business Media, 2005.

[53] P. G. Falkowski, M. E. Katz, A. H. Knoll, A. Quigg, J. A. Raven, O. Schofield, and F. Taylor, "The evolution of modern eukaryotic phytoplankton," *science,* vol. 305, no. 5682, pp. 354-360, 2004.

[54] P. Tréguer, C. Bowler, B. Moriceau, S. Dutkiewicz, M. Gehlen, O. Aumont, L. Bittner, R. Dugdale, Z. Finkel, and D. Iudicone, "Influence of diatom diversity on the ocean biological carbon pump," *Nature Geoscience,* vol. 11, no. 1, pp. 27-37, 2018.

[55] E. De Tommasi, "Light manipulation by single cells: the case of diatoms," *Journal of Spectroscopy,* vol. 2016, 2016.

[56] F. E. Round, R. M. Crawford, and D. G. Mann, *Diatoms: biology and morphology of the genera*. Cambridge university press, 1990.

[57] P. Kuczynska, M. Jemiola-Rzeminska, and K. Strzalka, "Photosynthetic pigments in diatoms," *Marine drugs,* vol. 13, no. 9, pp. 5847-5881, 2015.

[58] J. W. Goessling, S. Yanyan, M. Kühl, and M. Ellegaard, "Frustule photonics and light harvesting strategies in diatoms," *Diatom Morphogenesis,* pp. 269-300, 2021.

[59] L. R. Prelle, M. Albrecht, U. Karsten, P. Damer, T. Giese, J. Jähns, S. Müller, L. Schulz, L. Viertel, and K. Glaser, "Ecophysiological and cell biological traits of benthic diatoms from coastal wetlands of the southern Baltic Sea," *Frontiers in microbiology,* vol. 12, p. 642811, 2021.

[60] J. W. Goessling, Y. Su, P. Cartaxana, C. Maibohm, L. F. Rickelt, E. C. Trampe, S. L. Walby, D. Wangpraseurt, X. Wu, and M. Ellegaard, "Structure-based optics of centric diatom frustules: modulation of the in vivo light field for efficient diatom photosynthesis," *New Phytologist,* vol. 219, no. 1, pp. 122-134, 2018.

[61] M. Taniguchi and J. S. Lindsey, "Database of absorption and fluorescence spectra of> 300 common compounds for use in photochem CAD," *Photochemistry and photobiology,* vol. 94, no. 2, pp. 290-327, 2018.

[62] M. H. Tahersima, K. Kojima, T. Koike-Akino, D. Jha, B. Wang, C. Lin, and K. Parsons, "Deep neural network inverse design of integrated photonic power splitters," *Scientific reports,* vol. 9, no. 1, pp. 1-9, 2019.

[63] B. Shen, P. Wang, R. Polson, and R. Menon, "An integrated-nanophotonics polarization beamsplitter with 2.4× 2.4 μm2 footprint," *Nature Photonics,* vol. 9, no. 6, pp. 378-382, 2015.